J. Fluid Mech. (2022), *vol*. 944, A14, doi:10.1017/jfm.2022.460

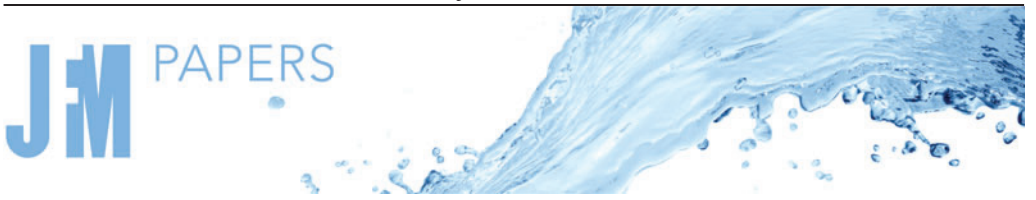

Structure and dynamics of a laminar separation bubble near a wing root: towards reconstructing the complete LSB topology on a finite wing

Connor E. Toppings[1] **and Serhiy Yarusevych**[1],†

[1]Department of Mechanical and Mechatronics Engineering, University of Waterloo, Waterloo, ON, Canada N2L 3G1

(Received 17 November 2021; revised 19 April 2022; accepted 17 May 2022)

The influence of the wing root junction on the laminar separation bubble forming on the suction surface of a semispan NACA 0018 wing cantilevered from the wind tunnel test section wall is studied using surface flow visualisations, particle image velocimetry and surface pressure measurements at a chord Reynolds number of 125 000 and an angle of attack of 6°. The test section wall boundary layer upstream of the wing is turbulent, and the spanwise influence of the junction on the separation bubble extends well beyond the test section wall boundary layer thickness. Substantial three-dimensionality is seen in the separation bubble flowfield near the wing root, where earlier transition and a reduction in separation bubble thickness is observed. In contrast with the wing tip, earlier transition and a reduction in separation bubble length occurs near the wing root. Outside of the junction affected region, the separation bubble is similar to separation bubbles forming on two-dimensional geometries, and displays mild spanwise waviness. The transition process away from the end affected regions is characterised by the formation of spanwise roll-up vortices that are shed in a nearly two-dimensional manner across the span. The analysis of the results shows that, near the wing root, the increased level of perturbations leads to earlier vortex roll-up and spanwise flow contributes to more rapid vortex breakdown. The results in the wing root region are complemented by the analysis of data from Toppings and Yarusevych (*J. Fluid Mech.*, vol. 929, 2021, A39) in the wing tip region to provide a more holistic outlook on the laminar separation bubble topology and dynamics on the entire finite wing.

Key words: boundary layer separation, vortex shedding, separated flows

† Email address for correspondence: syarus@uwaterloo.ca

1. Introduction

At relatively low chord Reynolds numbers, laminar boundary layers may persist over a substantial portion of a lifting surface (Carmichael 1981). If the boundary layer remains laminar downstream of the point of minimum pressure, laminar boundary layer separation may occur, and a laminar separation bubble (LSB) may form if the separated shear layer transitions to turbulence and reattaches, forming a thin region of recirculating flow (Tani 1964). For LSBs with small reverse flow velocities, transition occurs due to the convective amplification of disturbances in the separated shear layer through the Kelvin–Helmholtz instability mechanism, which leads to shear layer roll-up in the aft portion of the bubble (Watmuff 1999). If the reverse flow velocity or the height of the reverse flow exceed a certain threshold, absolute instability may occur (Alam & Sandham 2000; Rist & Maucher 2002). Because of their significant influence on wing performance at low chord Reynolds numbers ($7 \times 10^4 \lesssim Re_c \lesssim 5 \times 10^5$), LSBs have been the subject of numerous experimental (e.g. Gaster 1967; Brendel & Mueller 1988; Watmuff 1999; Simoni *et al.* 2017) and numerical investigations (e.g. Pauley, Moin & Reynolds 1990; Marxen, Lang & Rist 2013; Rodríguez & Gennaro 2019) on two-dimensional flow geometries. However, in many practical devices where LSBs occur, such as aircraft wings and low pressure gas turbine stages (e.g. Mueller & DeLaurier 2003; Hodson & Howell 2005), three-dimensional effects become significant at wing/blade tips and wall junctions. These end conditions are known to result in undesirable reductions in lift, while increasing drag, load fluctuations and acoustic emissions (e.g. Sieverding & Van den Bosche 1983; Bastedo & Mueller 1986; Simpson 2001; Moreau & Doolan 2016).

At $Re_c \gtrsim 10^4$, the attached laminar boundary layer on the suction side often becomes unstable, and the amplification of disturbances begins upstream of separation (Diwan & Ramesh 2009; Marxen *et al.* 2015; Michelis, Yarusevych & Kotsonis 2018). As these waves convect into the region of adverse pressure gradient, the Kelvin–Helmholtz instability gradually becomes the dominant amplification mechanism, with maximum disturbance growth rates occurring in the separated shear layer (e.g. Watmuff 1999; Diwan & Ramesh 2009). The ensuing rapid amplification of the most unstable perturbations leads to quasi-periodic roll-up of the separated shear layer into discrete vortices, which enhances the rate of wall-normal momentum transfer and enables reattachment in the mean sense (e.g. O'Meara & Mueller 1987; Watmuff 1999). On nominally two-dimensional geometries at low levels of freestream turbulence, the shear layer vortices are largely two-dimensional at formation (e.g. Nati *et al.* 2015; Kirk & Yarusevych 2017), but at higher levels of freestream turbulence, their spanwise coherence is reduced (e.g. Burgmann, Dannemann & Schröder 2008; Hosseinverdi & Fasel 2019). Amplification of the subharmonic of the fundamental instability frequency can lead to aperiodic merging between consecutive shear layer vortices, with vortex merging occurring more frequently in stronger adverse pressure gradients (Nati *et al.* 2015; Kurelek, Yarusevych & Kotsonis 2019; Lambert & Yarusevych 2019). Secondary (Marxen *et al.* 2013), absolute (Rodríguez, Gennaro & Juniper 2013) and global (Rodríguez & Theofilis 2010) instabilities, as well as the amplification of oblique instability waves (Michelis *et al.* 2018), have been identified as possible mechanisms for the onset of three-dimensionality in the shear layer vortices. Irrespective of the underlying mechanism, the ensuing vortex breakdown leads to the development of a turbulent boundary layer downstream of reattachment.

Three-dimensional end effects are known to influence LSB development on finite wings. In the immediate vicinity of the wing tip, downwash from the wing tip vortex suppresses boundary layer separation, leading to a delay in transition and eventual termination of the LSB (e.g. Bastedo & Mueller 1986; Huang & Lin 1995;

Chen, Qin & Nowakowski 2013; Awasthi, Moreau & Doolan 2018). In the region where three-dimensional tip effects are significant, localised bubble thickening and spanwise flow within the recirculation region have been observed by Toppings & Yarusevych (2021). Farther from the wing tip, LSB development on finite wings is similar to two-dimensional airfoils (Bastedo & Mueller 1986; Chen *et al.* 2013), with relatively small spanwise changes in the locations of separation and reattachment and the formation of largely two-dimensional shear layer vortices of constant frequency and wavelength (Toppings & Yarusevych 2021).

This article focuses on the LSB development on a finite wing in the proximity of the wing root, complementing the earlier work of the authors focused on the LSB topology and dynamics near a wing tip (Toppings & Yarusevych 2021). Fundamental aspects of flow development near the wing root junction have been considered in a number of previous studies (e.g. Roach & Turner 1985; Devenport & Simpson 1990; Schulz, Gallus & Lakshminarayana 1990; Wood & Westphal 1992; Fleming *et al.* 1993; Gand *et al.* 2010). Because of the momentum deficit in the test section wall boundary layer, wing sectional lift is reduced near the root (Wood & Westphal 1992). In addition, the presence of the wing leads to the reorientation of vorticity from the test section wall boundary layer into the streamwise direction, forming a horseshoe vortex system (Simpson 2001). The legs of the horseshoe vortices extend downstream on both sides of the wing, with opposite senses of streamwise vorticity. By promoting momentum exchange across the wing and test section wall boundary layers, the dominant horseshoe vortex increases skin friction in the vicinity of the junction (Simpson 2001). For the wing thickness Reynolds number $Re_T > 1000$, the horseshoe vortex is unsteady (Simpson 2001). The strength and size of the horseshoe vortex is influenced by the apparent bluntness of the wing, which is increased with increasing angle of attack. The additional drag on the wing due to the junction and the strength of the horseshoe vortex both increase with an increase in test section wall boundary layer thickness (Roach & Turner 1985; Fleming *et al.* 1993). Wings with relatively low bluntness may also experience corner separations, whereby both the wing and test section wall boundary layer separate in the vicinity of the junction (e.g. Schulz *et al.* 1990; Gand *et al.* 2010).

The majority of previous studies of wing root junction flows focused on the secondary flows created at the junction. In comparison, only a limited number of investigations have either directly or indirectly considered the influence of a wing root junction on LSB formation at low chord Reynolds numbers (e.g. Schulz *et al.* 1990; Huang & Lin 1995; Pelletier & Mueller 2001; Traub & Cooper 2008; Boutilier & Yarusevych 2012; Awasthi *et al.* 2018). Pelletier & Mueller (2001) examined the influence of end plates on the measured lift and drag coefficients of an Eppler 61 airfoil over the chord Reynolds number range $4.0 \times 10^4 \leq Re_c \leq 1.0 \times 10^5$, where laminar separation plays a dominant role in airfoil performance. They found that end plates increased drag and reduced lift. Surface pressure measurements within the test section wall boundary layer on an S8036 airfoil at chord Reynolds numbers within $7.5 \times 10^4 \leq Re_c \leq 2.0 \times 10^5$ were performed by Traub & Cooper (2008). They associated the decrease in sectional lift near a wing root junction with a substantial reduction in the leading edge suction peak, whereas the surface pressure farther downstream was less affected by the junction. The detrimental influence of junction effects on the performance of low Reynolds number wings can also be inferred from the results of Delafin, Deniset & Astolfi (2014), who conducted a three-dimensional unsteady Reynolds-averaged Navier–Stokes simulation of a wall-mounted NACA 66 airfoil at $Re_c = 7.5 \times 10^5$. They observed that the airfoil–wall junction caused a reduction in sectional lift coefficients over the portion of the span within $0.26c$ from the wall.

Insight into the three-dimensional topology of an LSB near a wing root is provided by the results of previous studies employing surface oil flow visualisations on wings and airfoils with LSBs. Huang & Lin (1995) conducted surface oil flow visualisations on a wall-mounted NACA 0012 semispan wing with an aspect ratio of $AR = 5$ at $Re_c = 8.0 \times 10^4$. At moderate angles of attack ($5 \leq \alpha \leq 7.1°$), an LSB formed on the suction surface. Although the locations of separation and reattachment were relatively uniform near the midspan of the wing, three-dimensional surface flow features were observed near the wing root. Specifically, a focus of separation appeared at the inboard end of the LSB separation line. Downstream of this focus, reattachment did not occur, producing a region of separated flow similar to a corner separation. As the angle of attack was increased, the focus of separation moved closer to the root, lengthening the spanwise extent of the LSB. The surface oil flow visualisations of Traub & Cooper (2008) also presented evidence of a focus of separation at the end of an LSB and corner separation downstream of the LSB near the wall junction.

Awasthi *et al.* (2018) studied a wall-mounted NACA 0012 semispan wing with $AR = 0.5$ at $Re_c = 2.74 \times 10^5$ using qualitative surface oil flow visualisations and quantitative local velocity measurements. The test section wall boundary layer thickness was 14 % of the wingspan or 58 % of the wing thickness. Although tip and root effects are expected to strongly influence each other at such a small aspect ratio, distinct changes in the flowfield were observed near both the root and tip. Junction effects were limited to within the test section wall boundary layer thickness, where laminar boundary layer separation from the wing was suppressed. Within the test section wall boundary layer, a component of spanwise flow away from the wing root was visible in the flow visualisations. Outside of the test section wall boundary layer, the LSB separation line was uniform along the span, whereas greater three-dimensionality was observed in the reattachment line, which shifted upstream near the wing tip. In contrast, the results of Boutilier & Yarusevych (2012) for a NACA 0018 airfoil at $Re_c = 1.0 \times 10^5$ suggest that wing end plate junction effects may influence LSB development beyond the end plate boundary layer thickness. By varying the end plate separation between $0.5c$ and $2.5c$, it was observed that reducing the spacing between the end plates caused non-monotonic changes to the airfoil surface pressure distribution near the midspan of the airfoil, well outside of the end plate boundary layers.

Previous studies suggest that the mean structure of an LSB, and consequently wing performance at low chord Reynolds numbers, is influenced by wing root and tip end effects. However, the underlying three-dimensional changes in the LSB topology and dynamics are yet to be elucidated, which motivates the present investigation. The objective of the present study is to provide a quantitative insight into the changes in the LSB topology and dynamics near a wing root, highlighting the spanwise changes that occur in the LSB and the associated transition process. This is achieved by performing an experimental investigation on a wall-mounted semispan NACA 0018 wing, employing surface pressure and both two- and three-component planar particle image velocimetry (PIV) measurements to quantify the three-dimensional LSB flowfield near the wing root.

2. Experimental methods

2.1. *Facility and model*

The LSB forming on the suction surface of a cantilevered wing with a semispan aspect ratio of $AR = 2.5$ was investigated using surface pressure measurements, surface oil flow visualisation and PIV. The experiments were conducted in the recirculating wind tunnel at

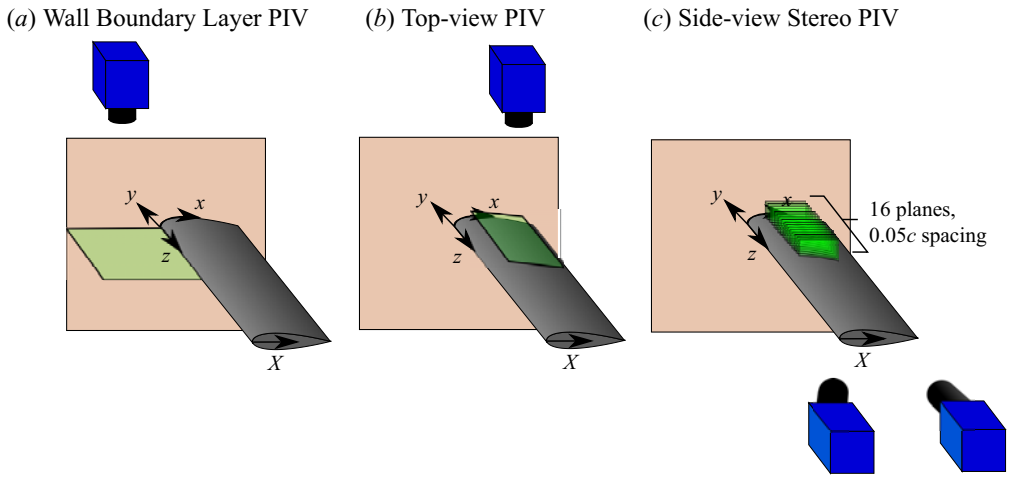

Figure 1. Coordinate axes and PIV measurement planes.

the University of Waterloo, which has a square test section with a side length of 0.61 m. The turbulence intensity in the centre of the empty test section measured using a single normal hot-wire anemometer and low-pass filtered at 10 kHz was less than 0.08 %. For surface pressure and PIV measurements, a rectangular aluminium NACA 0018 wing model with a chord length of $c = 0.20$ m was mounted to the sidewall of the test section, identical to the configuration used by Toppings & Yarusevych (2021). To produce an LSB on the suction surface with suitable size for PIV measurements, the wing was set at an angle of attack of $\alpha = 6^\circ$, and the freestream velocity was set to $U_\infty = 9.5\,\mathrm{m\,s^{-1}}$. The Reynolds number based on the wing chord length was $Re_c = 125\,000 \pm 4000$. Surface oil flow visualisations were performed on a plastic wing model of the same airfoil section, size, surface finish and position as the aluminium model to avoid contaminating embedded instrumentation in the aluminium wing model.

The results of side view PIV and surface oil flow measurements are presented using the surface-attached coordinate systems (x, y, z) shown in figure 1. Top-view PIV and surface pressure measurements are presented in a chord based coordinate system with the X axis parallel to the chord of the wing. In the surface attached coordinate system, the x axis is tangent to the suction surface of the wing and the y axis is normal to the suction surface. The z axis, which is parallel to the span, is common to both coordinate systems. The origin of both coordinate systems is at the wing root leading edge. For presentation of PIV measurements of the test section wall boundary layer, the negative x axis is defined parallel to the freestream in the region upstream of the leading edge.

2.2. *Measurement techniques*

Surface flow visualisations were performed by coating the suction side of the plastic wing model with a mixture of mineral oil and 10 µm hollow glass spheres. The mixture was brushed on the surface at zero free-stream velocity. Images of the oil mixture were acquired with a Nikon D7200 camera equipped with a 50 mm lens every 30 s for 1.5 h after starting the wind tunnel. As the oil film responded to the local surface shear stress, changes in local accumulation of bright hollow glass spheres on the dark model surface served to identify salient features in the surface flow topology in greyscale images.

Surface pressure measurements were obtained using 89 pressure taps distributed over the surface of the aluminium wing model. Centred at $z/c = 0.95$, 65 pressure taps arranged

in an alternating pattern between two chordwise rows separated in the spanwise direction by $0.05c$ were used to obtain the chordwise pressure distribution over the suction and pressure surfaces. The remaining 24 pressure taps were arranged in three spanwise rows on the suction surface at $X/c = 0.15$, 0.30 and 0.60. The pressure taps were connected through two Scanivalve multiplexers to two Setra Model 239 pressure transducers with input ranges of ± 250 Pa. Mean pressure measurements were obtained by sampling the pressure transducers for 4 s at 1000 Hz using a National Instruments USB-6259 data acquisition system, and the uncertainty in measured mean pressure coefficients is estimated to be ± 0.014 (95 % confidence).

Hot-wire measurements were used to characterise the spectral content of velocity fluctuations in the free stream and in the test section wall boundary layer. A single boundary-layer-type hot-wire probe was used with a constant temperature anemometer bridge. Hot-wire calibration was performed in the empty test section against the wind tunnel freestream velocity. The hot-wire signal was sampled at 25.6 kHz for 600 s, and hardware low-pass filtered at half the sampling frequency.

Non-intrusive velocity field measurements were performed using PIV in three different configurations illustrated in figure 1. In the first configuration, termed the wall boundary layer configuration, two-component PIV was used to characterise the test section wall boundary layer on the wall to which the wing model was mounted (figure 1*a*). In the second configuration, termed the top-view configuration, two-component PIV was performed on a plane tangent to but elevated from the wing surface (figure 1*b*). The top-view configuration was used to characterise the spanwise development of coherent structures in the LSB forming on the wing model. In the third configuration, termed the side-view configuration, stereo-PIV was used to investigate the three-dimensional velocity field of the LSB (figure 1*c*). For all PIV configurations, the flow was seeded with water–glycol fog particles, which were illuminated by a Photonics DM20-527 Nd:YLF pulsed laser. Velocity fields were computed using an iterative multi-pass cross-correlation algorithm with window deformation (Scarano & Riethmuller 2000) in the LaVision DaVis 10 software. Velocity vector outlier detection and removal was conducted using the universal outlier detection method (Westerweel & Scarano 2005). The correlation statistics method was used to estimate the uncertainty in instantaneous velocity measurements (Wieneke 2015). Uncertainties of quantities derived from the velocity measurements were calculated using the uncertainty propagation techniques of Sciacchitano & Wieneke (2016). Table 1 summarises the parameters of the three PIV configurations.

The test section wall boundary layer was measured in a plane intersecting the leading edge of the wing and parallel to the freestream (figure 1*a*), using a single Photron FastCam SA4 1 Mpx camera operating in double frame mode at 100 Hz. A total of 2728 instantaneous velocity fields were acquired, for a total sampling time of 27.28 s. The frame separation was 36 µs, and the particle displacement in the freestream was 13 px. The camera was fitted with a 200 mm Nikon fixed focal length macro lens, resulting in a field of view that extended $0.1c$ upstream of the leading edge and $0.1c$ in the spanwise direction. The forming optics for the light sheet in the test section wall boundary layer configuration were located outside of the test section. Particle images were pre-processed using sliding minimum subtraction and sliding spatial intensity normalisation. The initial and final window sizes used in the iterative vector calculation procedure were 64 px × 64 px and 16 px × 16 px, respectively. With 75 % overlap between the final windows, the resulting vector pitch was $5.3 \times 10^{-4}c$. The uncertainty (95 % confidence) due to random errors in the instantaneous velocity measurements within the test section wall boundary layer was estimated to be less than 5 % of the freestream velocity for both the streamwise (u)

https://doi.org/10.1017/jfm.2022.460 Published online by Cambridge University Press

Parameter	Test section wall boundary layer	Top-view		Side-view	
Cameras	(One) Photron FastCam SA4	(One) LaVision Imager sCMOS	(One) Photron FastCam SA4	(Two) LaVision Imager sCMOS	
Sensor size	1024 px × 1024 px	2560 px × 1024 px	1024 px × 1024 px	2560 px × 1024 px	
Field of View	$0.10c \times 0.10c$	$0.60c \times 0.70c$	$0.70c \times 0.70c$	$0.3c \times 0.08c$	
Lens focal length	200 mm	50 mm		200 mm	
Sampling frequency (non-phase-locked)	100 Hz	25 Hz	1940 Hz	52.35 Hz	
Sampling frequency (phase-locked)		24.56 Hz		49.13 Hz	
Sampling time (non-phase-locked)	27.3 s	40.0 s	1.4 s	19.1 s	
Sampling time (phase-locked)		10.2 s		5.1 s	
Angle between optical axes				35°	
Frame separation	36 µs	50 µs	36 µs	36 µs	
Freestream particle displacement	13 px	9 px	3 px	20 px	
Initial interrogation window size	64 px × 64 px	64 px × 64 px	64 px × 64 px	24 px × 24 px	
Vector pitch	$0.00053c$	$0.001c$	$0.003c$	$0.00048c$	
				Downstream camera	Upstream camera
Aperture	$f/11$	$f/2$	$f/1.4$	$f/4$	$f/5.6$
Magnification factor	0.76	0.12	0.15	0.253	0.246
Light source	Photonics DM20-527 Nd:YLF Pulsed Laser				
Light sheet thickness	$\approx 0.01c$				
Particles	Water–glycol fog				
Final interrogation window overlap	75 %				
Final interrogation window size	16 px × 16 px				

Table 1. PIV measurement parameters.

and spanwise (w) velocity components. The maximum uncertainty occurred along the test section wall due to light reflections.

For the top-view PIV configuration (figure 1*b*), the light sheet was positioned to intersect the top halves of the shear layer vortices shed from the LSB. Particle images were acquired using a single LaVision Imager sCMOS 5.5 Mpx camera operating at 23.05 Hz for low-speed measurement of statistical quantities, and using a single Photron FastCam SA4 1 Mpx camera operating at 1940 Hz for high-speed measurement of fluctuating velocity spectra. For both camera set-ups, a 50 mm Nikon fixed focal length lens was used, resulting in a field of view extending $0.60c$ and $0.70c$ in the X direction and $0.70c$ and $0.70c$ in the z direction for the high-speed and low-speed cameras, respectively. The forming optics for the light sheet in the top-view configuration were located outside of the test section. Particle images were pre-processed using sliding minimum subtraction and sliding spatial intensity normalisation. The initial and final window sizes used in the iterative vector calculation procedure were 64 px × 64 px and 16 px × 16 px, respectively. With 75 % overlap between the final windows, the resulting vector pitch was $0.001c$ and $0.003c$ for the low-speed and high-speed cameras, respectively. A total of 1000 images was recorded with the low-speed camera, and 2728 images with the high-speed camera, for total sampling times of 40.0 and 1.4 s, respectively. Outside of the test section wall boundary layer, the uncertainty (95 % confidence) due to random errors in the instantaneous velocity measurements from the low-speed camera was estimated to be less than 10 % of the freestream velocity for both the streamwise (u) and spanwise (w) velocity components. The maximum uncertainty occurred near the test section wall due to light reflections.

To investigate the three-dimensional velocity field of the LSB near the wing–wall junction, stereo-PIV was performed in a series of side-view x–y planes near the wing root (figure 1*c*), using two LaVision Imager sCMOS 5.5 Mpx cameras. The cameras were equipped with 200 mm fixed focal length macro lenses and Scheimpflug adapters, with a 35° included angle between the optical axes of each camera. The apertures of the two cameras were adjusted to reduce differences in image intensity due to forward and backward light scattering from the fog particles (table 1). After cropping both camera sensors to 2560 px × 1024 px, the combined image field of view was $0.3c \times 0.08c$. The cameras and light sheet optics were mounted on computer controlled traverses providing synchronised translation of the side-view imaging plane in the z direction. Measurements were taken at 16 planes over the range $0.10 \leq z/c \leq 0.85$, with a spanwise distance of $0.05c$ between consecutive measurement planes, as illustrated in figure 1(*c*). The forming optics for the light sheet were located in the test section approximately $8c$ downstream of the wing, and verified to have no measurable influence on the pressure distribution on the wing. Because of light reflections from the test section wall and physical constraints in positioning the light sheet optics within the test section, side-view measurements could not be performed at $z/c < 0.10$. Particle images were acquired in double frame mode at 52.35 Hz with 36 µs separation between frames. A physical calibration using a three-dimensional calibration plate was performed at the first measurement plane in the spanwise traverse of the side-view stereo-PIV system. Then, self-calibration was performed for all measurement planes using the first 100 particle images at each plane (Wieneke 2005). Prior to velocity field calculations, particle images were pre-processed using sliding minimum subtraction and normalised by the average of all images at each plane. The initial and final window sizes used in the iterative vector calculation procedure were 24 px × 24 px and 16 px × 16 px, respectively. With 75 % overlap between windows, the resulting vector pitch was $4.8 \times 10^{-4}c$. A total of 1000 instantaneous velocity measurements were obtained at each measurement plane, for a total sampling time

of 19.10 s. The final side-view velocity vector fields were interpolated onto the surface attached x–y–z coordinate system (figure 1). The uncertainty (95 % confidence) due to random errors in the instantaneous velocity measurements within the LSB was estimated to be less than 2 %, 2 % and 10 % of the freestream velocity for the streamwise (u), wall-normal (v) and spanwise (w) velocity components, respectively.

In addition, phase-locked PIV measurements were performed using the top-view and side-view configurations to correlate velocity measurements taken in different measurement planes. As vortex shedding from an LSB is quasi-periodic (Häggmark, Bakchinov & Alfredsson 2000), weak acoustic excitation was used to regularise the vortex shedding and provide a phase reference for the PIV system (e.g. Kurelek *et al.* 2021). The acoustic excitation was produced by a speaker in the test section located six chord lengths downstream of the wing model. The speaker was driven with a sine wave signal at the central instability frequency of $16.5U_\infty/c$ determined using high-speed PIV in the natural flow. The acoustic forcing resulted in an increase in the sound pressure level at the surface of the wing of 0.8 dB from the sound pressure level of 84.9 dB in the natural flow. The amplitude of the excitation was selected such that it produced no measurable changes in the mean flow, as verified by surface pressure and PIV measurements.

2.3. *Test section wall boundary layer*

The test section wall boundary layer was characterised from PIV measurements performed in the configuration depicted in figure 1(a). The obtained streamwise mean and root-mean-square (RMS) fluctuating velocity profiles of the test section wall boundary layer at $x/c = -0.100$ and $x/c = -0.025$ are plotted in figure 2(a), and mean streamwise velocity contours illustrating the development of the test section wall boundary layer upstream of the leading edge are shown in figure 2(b). At $x/c = -0.100$, the test section wall boundary layer has a thickness of $\delta_{99x} = 0.032c$ and a shape factor of 1.89. Both the local shape factor value and the relatively high level of velocity fluctuations point to the turbulent nature of the test section wall boundary layer at the model location. The results also show that the adverse pressure gradient induced by the presence of the wing leads to a notable flow deceleration. The $\overline{u} = 0$ contour in figure 2(b) and the reverse flow near the wall at $x/c = -0.025$ in figure 2(a) indicate that this induces test section wall boundary layer separation upstream of the wing, suggesting the presence of a horseshoe vortex system at the wing root. The shift in the z/c location of the maximum RMS velocity fluctuations away from the wall between $x/c = -0.100$ and -0.025 (figure 2a) also points to the presence of a separated shear layer and horseshoe vortex, with the associated increase in the magnitude of velocity fluctuations. The results show that the wall normal extent of the wall-bounded shear layer upstream of the leading edge of the wing is confined well within $z/c < 0.04$. Thus, both pressure and velocity measurements performed on the wing model in the present investigation, which begin at $z/c = 0.25$ and 0.10, respectively, are located outside of the direct extent of the test section wall boundary layer.

Figure 2(c) presents the power spectral density ($\mathcal{F}_{u'u'}$) of streamwise velocity fluctuations measured in the empty test section at the model location. The power spectral density of the hot-wire signal was estimated using Welch's method (Welch 1967) with a window size of 2^{17} samples. The resulting uncertainty in the power spectral density is less than 15 %, and the frequency resolution is $0.004U_\infty/c$. Spectra are presented for the test section wall boundary layer at $z/c = 0.032$ (equivalent to $z = \delta_{99x}$ with the wing model installed) and in the freestream. The results reveal a broadband spectrum in the test section wall boundary layer, typical of turbulent shear flows. The wall boundary layer spectrum is devoid of any significant peaks, however there is a notable increase in the energy content

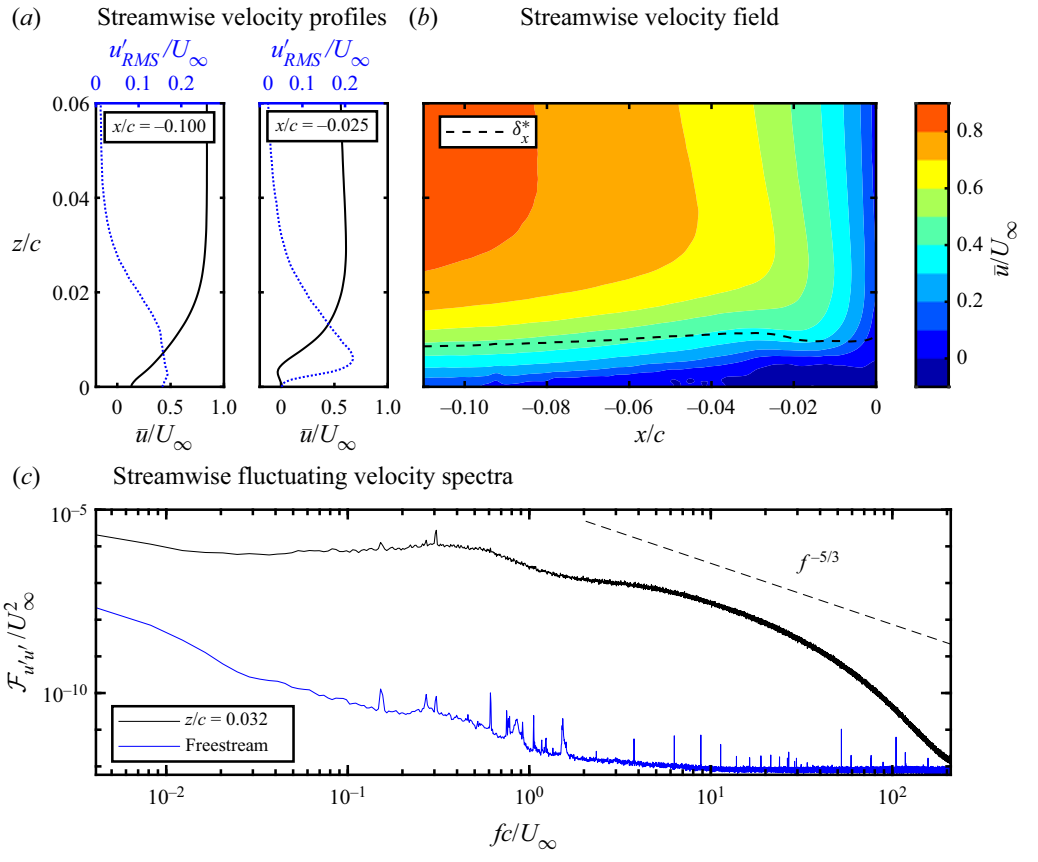

Figure 2. (*a*) Test section wall boundary layer mean and RMS velocity profiles. (*b*) Test section wall boundary layer streamwise velocity field upstream of wing. (*c*) Fluctuating velocity spectra in the test section wall boundary layer at $z/c = 0.032$ and in the freestream.

compared with the level of freestream perturbations, also reflected in significant velocity fluctuations in the near-wall region seen in figure 2(*a*). Therefore, the initial amplitudes of disturbances in the wing boundary layer are expected to increase near the wing root, which, in addition to the global changes in the pressure gradient, may influence transition and, hence, LSB development near the wing root junction.

3. Results

3.1. *Mean separation bubble flowfield*

The surface pressure measurements presented in figure 3 provide a global perspective on the flow development over the wing model. As evidenced by the virtually identical pressure distributions of the natural and weakly excited flows, the mean flowfields of the two cases are closely matching, which was also verified with PIV data. Therefore, the following discussion of the mean LSB development only presents results from the natural flow for brevity. The presence of a typical short LSB on the suction surface can be inferred from the chordwise mean pressure distribution at $z/c = 0.95$ (figure 3*a*). A pressure plateau begins near $X/c \approx 0.20$, indicating laminar boundary layer separation, and ends near $X/c \approx 0.45$, where turbulent reattachment leads to a rapid pressure recovery.

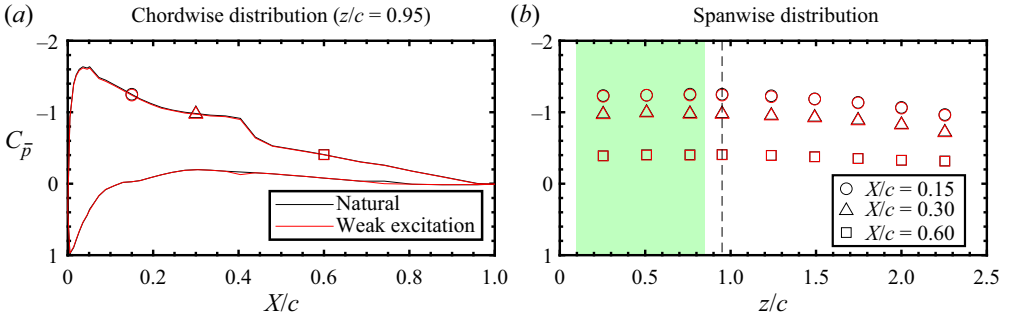

Figure 3. (*a*) Chordwise and (*b*) spanwise pressure distributions. The locations of the spanwise pressure taps in (*b*) are indicated by the markers in (*a*). Dashed line in (*b*) indicates spanwise location of chordwise pressure measurements shown in (*a*). Shaded region indicates spanwise range of side-view PIV measurements.

The spanwise pressure distribution in figure 3(*b*) shows a reduction in suction near the wing tip, whereas no significant spanwise pressure variation is seen near the wing root within $0.25 \leq z/c \leq 0.95$. It suggests that the chordwise pressure distribution at $z/c = 0.95$ (figure 3*a*) is representative of the majority of the region covered by side-view PIV measurements near the wing root. The LSB on this portion of the wing is expected to be similar to an LSB forming on a two-dimensional airfoil at the same effective angle of attack (Bastedo & Mueller 1986). Figure 4 confirms this, showing the mean streamwise velocity field at the farthest plane from the wing root ($z/c = 0.85$, figure 4*a*) in comparison with measurements on a two-dimensional NACA 0018 airfoil section at similar effective ($\alpha = 5^\circ$, figure 4*b*) and geometric ($\alpha = 6^\circ$, figure 4*c*) angles of attack. The spatial extent of the LSB can be assessed from the darkest blue contour, which indicates the area of reverse flow, and the triangle markers, which indicate separation and reattachment. The reduction in effective angle of attack on the $AR = 2.5$ wing leads to a reduction in the streamwise adverse pressure gradient, delaying transition in the separated shear layer and lengthening the LSB on the wing (figure 4*a*) relative to the LSB on the two-dimensional airfoil at the same geometric angle of attack (figure 4*c*). The locations of maximum displacement thickness and reattachment on the wing at $\alpha = 6^\circ$ are similar to, but slightly upstream of those from the LSB on the airfoil at a similar effective angle of attack ($\alpha = 5^\circ$, figure 4*b*). The difference in the streamwise locations of separation and maximum displacement thickness are within the experimental uncertainty, and the difference in the location of reattachment is of similar magnitude to the spanwise variations commonly seen in nominally two-dimensional LSBs (e.g. Miozzi *et al.* 2019; Kurelek *et al.* 2021). The two-dimensionality of the LSB forming near the midspan of the wing suggests negligible interaction between root and tip effects for aspect ratios equal to or greater than that of the present wing model.

Mean streamwise and spanwise velocity fields from selected planes near the wing root are presented in figure 5. In the range $0.15 \leq z/c \leq 0.80$, relatively small variations in bubble thickness and the locations of separation, transition, and reattachment are observed (figure 5*a*). The overall LSB structure remains similar to that seen on the two-dimensional airfoil section at a similar effective angle of attack (figure 4*b*). However, LSB parameters at $z/c = 0.10$ are strikingly different from the planes farther away from the wing root. Here, the streamwise and wall-normal extent of the reverse flow region are substantially reduced, and reattachment occurs at nearly the same x/c location as the maximum streamwise displacement thickness. These results indicate that the wing–wall junction strongly influences LSB development much farther from the wing root than the

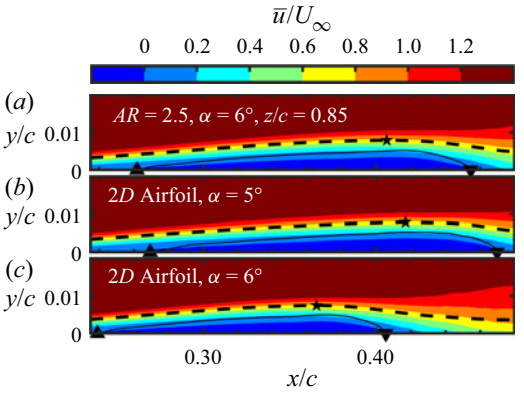

Figure 4. Comparison of mean streamwise velocity field on airfoil and $AR = 2.5$ wing. Dashed line: δ_x^*; solid line: zero-net streamwise mass flux line; star: maximum δ_x^*; ▲ and ▼: separation and reattachment locations. Data in (*b*) from Toppings, Kurelek & Yarusevych (2021) and data in (*c*) from Toppings & Yarusevych (2021).

thickness of the test section wall boundary layer ($\delta_{99x} \approx 0.032c$, figure 2*b*). The increasing three-dimensionality of the LSB flowfield near the wing root is revealed by the contours of spanwise velocity in figure 5(*b*), which show a strong spanwise flow in the positive z direction in the aft portion of the LSB for $z/c \leq 0.30$. This three-dimensional flow is likely related to the earlier reattachment observed near the wing root. Farther away from the wing root, spanwise flow within the LSB diminishes, consistent with the spanwise uniformity in the pressure field measured outside of the immediate vicinity of the wing–wall junction (figure 3*b*). As the most pronounced junction effects occur within the region $z/c \leq 0.2$, this region is termed the junction region in the remaining discussion.

The mean surface topology of the LSB near the wing root is explored in figure 6(*a*). The shown limiting streamlines were calculated using the fourth-order Runge–Kutta method applied to the linearly interpolated near-wall velocity gradient. The three-dimensional separation and reattachment lines, identified heuristically as the envelopes of nearby limiting streamlines, are denoted by the thick solid and dashed lines, respectively. For $z/c \lesssim 0.50$, a substantial spanwise flow directed away from the wing root is observed within the LSB, particularly within the aft portion of the bubble. The spanwise flow within the bubble near the wing root suggests that the three-dimensional LSB opens near the wing root, allowing fluid to enter into the mean recirculation region. Sufficiently far from the wing root junction, for $z/c \gtrsim 0.5$, relatively minor variations in the spanwise component of the limiting streamlines are observed, similar to those seen in nominally two-dimensional LSBs (e.g. Diwan & Ramesh 2009; Miozzi *et al.* 2019).

The topological description of three-dimensional flow separation requires that global separation lines emanate from saddle points and terminate at nodes or foci of separation (e.g. Surana, Grunberg & Haller 2006). The presence of a focus of separation (F) can be inferred near ($x/c = 0.34$, $z/c = 0.10$) in figure 6(*a*). The location of the focus is consistent with the increase in positive spanwise velocity with increasing x/c near the wing surface between $x/c = 0.3$ and $x/c = 0.4$ at $z/c = 0.10$ in figure 5(*b*). On the separation line, a saddle point (S) is seen at ($x/c = 0.28$, $z/c = 0.12$) (figure 6*a*) which is likely connected to the nearby focus, meaning that separation near the wing root can be classified as a global separation (e.g. Tobak & Peake 1982).

The observed changes in surface topology in the junction region (figure 6*a*) bear notable similarities and differences to the LSB topology near the wing tip (Toppings & Yarusevych 2021), depicted in figure 6(*b*) for comparison. At both the wing tip and wing root, fluid

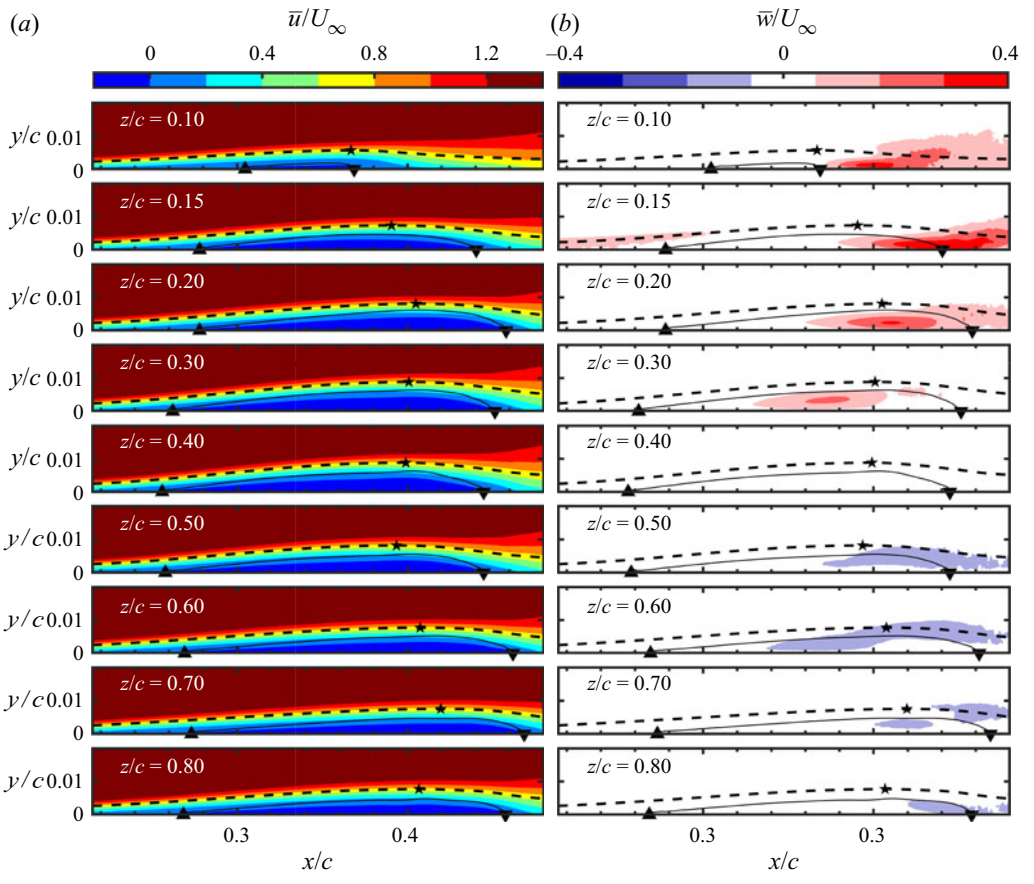

Figure 5. Contours of mean streamwise and spanwise velocity at selected planes on the $AR = 2.5$ wing. Dashed line: δ_x^*; solid line: zero-net streamwise mass flux line; star: maximum δ_x^*; ▲ and ▼: separation and reattachment locations.

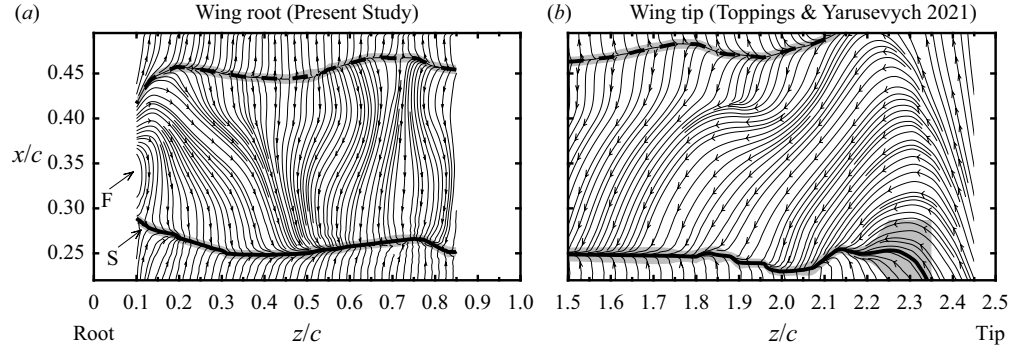

Figure 6. Limiting streamlines near (*a*) wing root, (*b*) wing tip (adapted from Toppings & Yarusevych (2021), figure 10). Thick solid line: separation line; thick dashed line: reattachment line; shaded areas: uncertainty in separation and reattachment lines.

enters into the recirculation region in the aft part of the LSB and a substantial spanwise flow develops, which gradually diminishes towards the midspan of the wing, away from the direct influence of end effects. However, the spanwise extent of the influence of the wing

tip is much larger than the root, as evidenced by the predominant spanwise component of the limiting streamlines across the majority of figure 6(*b*). This correlates with the large extent of the spanwise pressure gradient region near the wing tip (figure 3*b*). A notable downstream shift in reattachment occurs near the wing tip (figure 6*b*) compared with the upstream movement of reattachment near the wing root (figure 6*a*), likely related to the reduction in streamwise adverse pressure gradient (figure 3*b*) and associated reduction in effective angle of attack near the wing tip (Bastedo & Mueller 1986). In contrast to the wing root, where the LSB separation line is a global separation line emanating from a saddle point, separation near the wing tip (figure 6*b*) is a local separation, because the separation line arises from a gradual convergence of ordinary limiting streamlines (Tobak & Peake 1982).

The surface oil flow visualisation after 1.5 h of wind tunnel operation is shown in figure 7(*a*), and a time lapse of the entire visualisation is available in Movie 1. Boundary layer separation can be inferred from the local accumulation of oil–powder mixture near $x/c = 0.20$. Reattachment can be detected where less-pronounced oil accumulation occurs around $x/c = 0.45$, followed by a uniform oil distribution downstream in the developing turbulent boundary layer, similar to the results of Selig, Deters & Wiliamson (2011). The flow visualisation results agree well with the topology revealed by the limiting streamlines calculated from PIV measurements, with minor variations attributed to experimental uncertainty and unavoidable, minute differences in models and angles of attack settings between the two experiments. A schematic interpretation of the surface oil flow image is presented in figure 7(*b*), which was constructed with the aid of Movie 1. The revealed LSB topology is analogous to and confirms that inferred from the PIV data. Specifically, a focus of separation (F) can be inferred in the junction region, with a sense of rotation that is consistent with spanwise inflow into the aft portion the LSB. Near the wing tip, no well-defined critical points are found, and a downstream shift in reattachment occurs. These features were also reported in the surface topology sketch based on surface oil flow visualisation of Huang & Lin (1995) on a cantilevered NACA 0012 wing with $AR = 5.0$ at $Re_c = 8.0 \times 10^4$ and $\alpha = 5.0^\circ$, which is reproduced in figure 7(*c*). The overall similarity between results from different experiments involving different airfoil profiles and flow conditions suggests that the topological changes in the LSB structure near the wing root observed in the present study represent a general LSB topology near a wing root junction.

In addition to the surface topology, the wall-normal extent of the LSB is also affected by the wing root junction. The height of the core of the separated shear layer and the thickness of the reverse flow region as measured using the side-view PIV configuration are depicted in figure 8 by the maximum streamwise displacement thickness and maximum height of the $\overline{u} = 0$ contour, respectively. The present results from the wing root region are complemented by the wing tip data from Toppings & Yarusevych (2021). Both parameters yield similar spanwise trends in the wall-normal extent of the LSB. Near the midspan of the wing, changes in the thickness of the LSB are relatively gradual, and a progressive thickening of the LSB with increasing z/c can be inferred. Approaching the wing root, a local maximum in the bubble height occurs at $z/c = 0.35$. At lower z/c locations, the progressive increase in three-dimensional effects is accompanied by a significant reduction in the bubble height. An extrapolation of the rapidly decreasing bubble height for $z/c < 0.20$ suggests that the LSB is eventually eliminated by junction effects at a short distance inboard from $z/c = 0.10$. Because a reduction in the distance of an inflectionally unstable shear layer from a surface causes a reduction in the growth rates of unstable disturbances (Michalke 1991), substantial changes in the stability and transition process of the separated

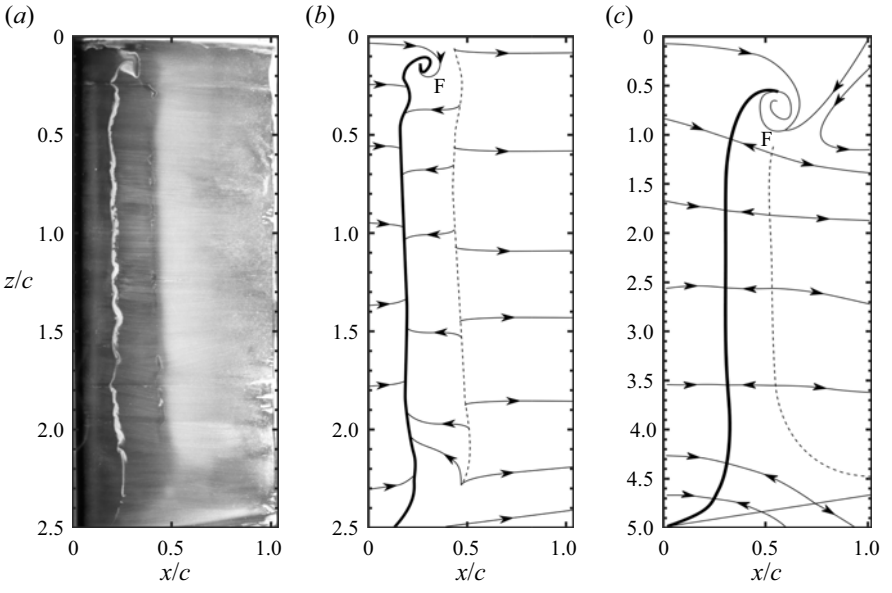

Figure 7. (*a*) Surface oil flow visualisation, present study. Full time lapse in supplementary movie 1 available at https://doi.org/10.1017/jfm.2022.460. (*b*) Surface topology schematic, present study. (*c*) Surface topology schematic adapted from Huang & Lin (1995) on a NACA 0012 wing at $Re_c = 8.0 \times 10^4$ and $\alpha = 5.0°$. Thick lines: separation lines; dashed lines: reattachment lines.

laminar shear layer are expected to occur near the wing root, which will be explored in § 3.2. Also plotted in figure 8 is the minimum mean streamwise velocity $\overline{u}_{min}/U_\infty$, which indicates the strength of reverse flow within the LSB. Over a majority of the span, the minimum mean streamwise velocity magnitude varies between approximately 5 % and 10 % of the freestream velocity, which suggests that the primary instability mechanism is convective in nature. The displacement thickness Reynolds numbers in the present LSB are less than 1000, for which Alam & Sandham (2000) calculated that the reverse flow magnitude required for absolute instability is greater than 15 % of the freestream velocity. Further, the ratio of the height of the $\overline{u}/U_\infty = 0$ contour to the streamwise displacement thickness in the present LSB is less than 0.56 at all locations, which is below the threshold of approximately 0.6 required for absolute instability in the work of Rist & Maucher (2002) at comparable Reynolds numbers and reverse flow velocities. Finally, for all spanwise locations, except at $z/c = 2.10$, LSB cross sections do not satisfy the criterion proposed by Avanci, Rodríguez & Alves (2019) that requires the inflection point of the velocity profile to be located below the zero-net streamwise mass flux line for absolute instability to occur. Therefore, the primary instability in the junction and midspan regions is expected to be convective in nature. Although the identification of global instability modes is outside the scope of this work, the reverse flow does exceed the threshold required for the stationary global instability identified by Rodríguez & Theofilis (2010), which may be responsible for the spanwise waviness seen in the LSB, similar to that reported by Rodríguez & Gennaro (2019).

Similar to the trend seen in the junction region, a monotonic decrease in bubble thickness also occurs near the wing tip for $2.00 < z/c < 2.30$, and at $z/c = 2.00$ the bubble thickness reaches a local maximum. This suggests that both types of end conditions cause the thickness of the reverse flow region and height of the separated shear layer to

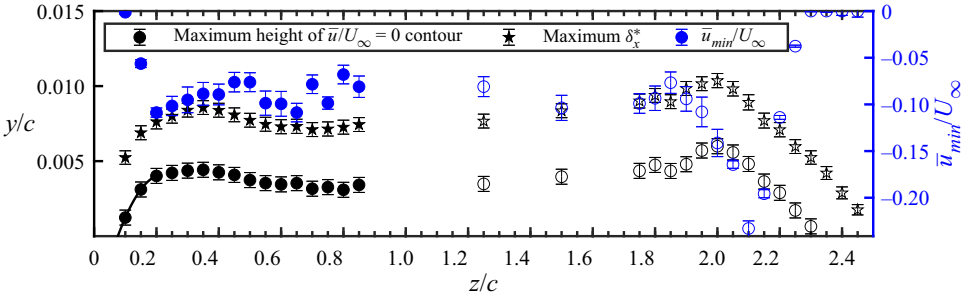

Figure 8. Maximum displacement thickness, maximum height of $\overline{u}/U_\infty = 0$ contour and minimum streamwise velocity at each side-view measurement plane. Solid markers: present study; open markers: Toppings & Yarusevych (2021); solid line: extrapolation of maximum height of $\overline{u}/U_\infty = 0$ contour.

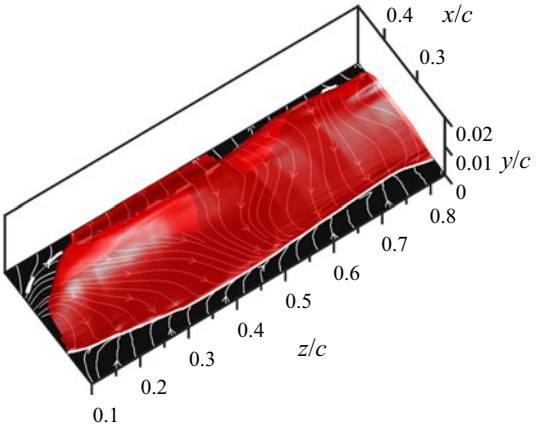

Figure 9. Three-dimensional mean LSB structure near the wing root. Red surface: separation streamsurface; thin lines: limiting streamlines; thick solid line: separation line; thick dashed line: reattachment line.

increase near the open ends of the LSB, prior to the onset of the reduction in bubble thickness induced by the end conditions.

The three-dimensional structure of the time-averaged LSB near the wing root is depicted in figure 9, which presents the separation streamsurface in red and the limiting streamlines on the surface of the wing in white. The separation streamsurface is defined as the surface formed from the set of streamlines that emanate from the separation line. The separation streamsurface was calculated using linear interpolation of the stereo-PIV velocity data and streamline integration using the fourth-order Runge–Kutta method. The figure shows that the streamwise extent of the LSB shortens notably in the junction region for $z/c \leq 0.20$, where the separation surface is swept into the recirculation region in the aft part of the LSB by spanwise flow (figure 5*b*), and the reattachment line shifts upstream. At the same time, for $z/c > 0.20$, the mean LSB structure features relatively small spanwise undulations in the locations of separation and reattachment. Similar spanwise variations in mean LSB characteristics have been also reported for nominally two-dimensional flow configurations (Rodríguez & Theofilis 2010; Kurelek *et al.* 2021).

The foregoing analysis of flow visualisation results and velocity measurements suggests that the LSB on the wing is an open bubble that contains substantial spanwise flow of varying magnitude near the wing root (figure 5*b*) and tip

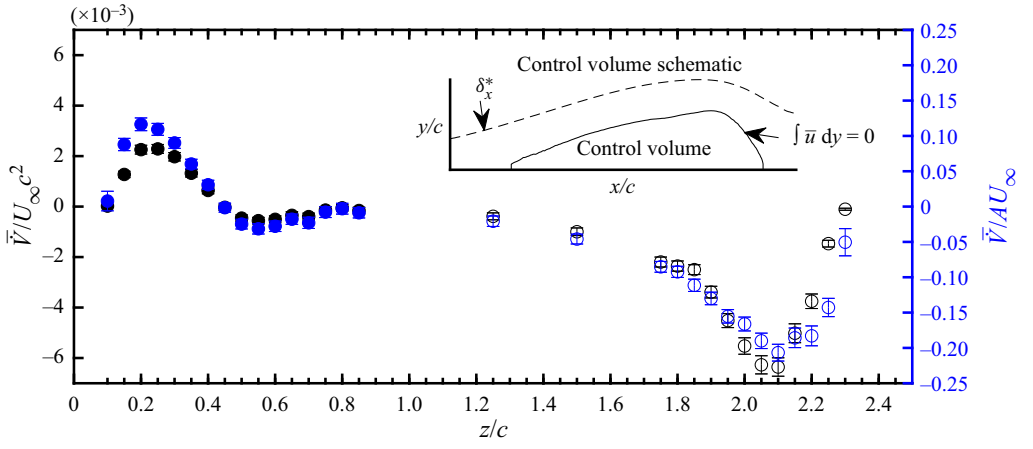

Figure 10. Spanwise volume flux (black) and mean spanwise velocity (blue) through area enclosed by zero-net streamwise mass flux line. Solid markers: present study; open markers: Toppings & Yarusevych (2021).

(Toppings & Yarusevych 2021, figure 9). Note that the presence of a three-dimensional reattachment line at a given z location does not preclude the exchange of fluid between the recirculation region of a three-dimensional separation bubble and the surrounding flow at that location, as elaborated on by Kremheller & Fasel (2010) and Toppings & Yarusevych (2021). Further insight into the three-dimensional mean LSB flowfield is provided by figure 10, which plots the spanwise volume flow rate ($\overline{\dot{V}}$) through the area (A) enclosed by the zero-net streamwise mass flux line (Horton 1968) (figure 10 inset) at each side-view PIV measurement plane. Because the spanwise volume flow rate is a function of the LSB cross-sectional area, which also varies along the span of the wing, the mean spanwise velocity ($\overline{\dot{V}}/A$) is also presented in the figure. Estimates near the wing tip are obtained using data from Toppings & Yarusevych (2021).

In the junction region, the inflow of fluid into the recirculation region leads to a positive spanwise volume flow rate, consistent with the positive spanwise velocity contours in the aft portion of the LSB near the wing root in figure 5(*b*). The largest spanwise volume flow rate is reached at $z/c = 0.20$, with the subsequent decrease seen towards the midspan. For $0.4 \leq z/c \leq 0.85$, the spanwise volume flux within the LSB is nearly zero, as expected given the similarity between the LSB on the wing and a two-dimensional LSB in this region (figure 4). Near the midspan ($z/c = 1.25$), a negative spanwise volume flow rate develops inside the LSB due to the spanwise pressure gradient induced by the tip effects (figure 3*b*). As the spanwise pressure gradient intensifies towards the wing tip, an increasingly negative spanwise volume flow rate develops, peaking at $z/c = 2.10$, before diminishing to zero as the LSB becomes thinner near the wing tip (figure 8). The mean spanwise velocity within the LSB displays a similar spanwise distribution to that of the mean spanwise volume flow rate. This suggests that the observed changes in the spanwise volume flow rate are linked to changes in both LSB cross-sectional area and spanwise velocity, which can be confirmed by comparing figures 5 and 10. The occurrence of local maxima in the magnitude of the mean spanwise volume flow rate and mean spanwise velocity near both the wing root and tip point to a similar mean LSB structure at both types of end conditions.

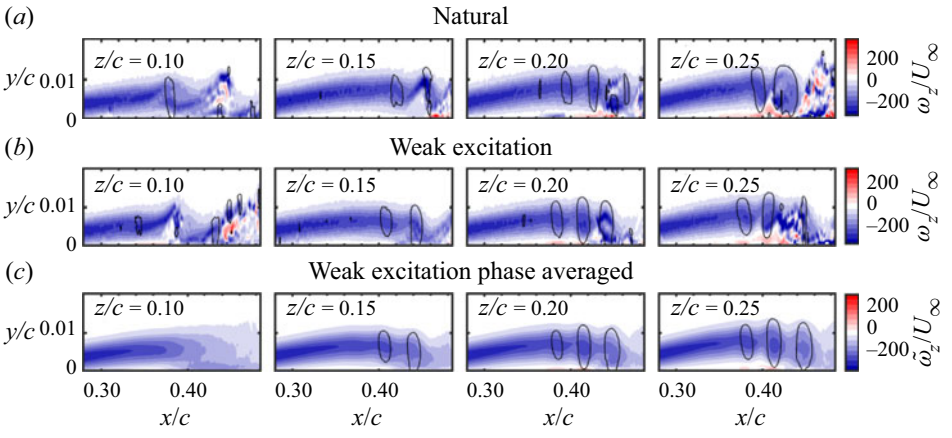

Figure 11. Spanwise vorticity contours at the four side-view planes closest to the wing root: (*a*) uncorrelated snapshots from natural flow, (*b*) phase-locked snapshots from weakly excited flow and (*c*) phase average from weakly excited flow.

3.2. *Separation bubble dynamics near the wing root*

The inherent relation between the separated shear layer dynamics and mean bubble topology suggests that the notable changes observed in the latter near the wing root are accompanied by substantial changes to the former. This is illustrated in figure 11, which presents contours of instantaneous spanwise vorticity (figures 11(*a*) and 11(*b*)), and phase-averaged vorticity (figure 11*c*) at an arbitrary but constant phase across the four side-view measurement planes closest to the wing root. For $z/c \geq 0.15$, the snapshots from the natural and weakly excited flows depict the development of spanwise vortices in the shear layer, which is typical of two-dimensional LSBs (e.g. Häggmark *et al.* 2000; Hain, Kähler & Radespiel 2009) and of the present LSB at the planes outside of the junction and tip affected regions. With decreasing z/c, the separated shear layer moves closer to the wing surface, as the LSB becomes thinner under the influence of the wing root junction. At $z/c = 0.10$, roll-up of the shear layer occurs farther upstream. The earlier formation of vortical structures at $z/c = 0.10$ is indicative of earlier transition and consistent with the upstream shift in mean reattachment at this spanwise location (figure 6*a*). In addition, at $z/c = 0.10$, the shed vortices lose coherence more rapidly as they break down to turbulence, which leads to the absence of well-defined vortices in the phase-averaged results at $z/c = 0.10$ (figure 11*c*). This is attributed to the more pronounced influence of three-dimensional junction effects near the wing root, where disturbances are introduced from the turbulent test section wall boundary layer, and where strong mean spanwise flow is present in the aft portion of the LSB (figure 5*b*). It is of interest to note that the LSB dynamics in the junction region differs from that reported near the wing tip, where a progressive reduction in the strength of the shear layer vortices and delay in transition take place (Toppings & Yarusevych 2021, figures 17 and 18).

The spanwise velocity measurements corresponding to the results presented in figure 11 are explored in figure 12. The instantaneous snapshots (figures 12(*a*) and 12(*b*)) reveal that substantial spanwise velocity fluctuations occur during shear layer vortex formation and breakdown in the aft portion of the LSB. Because the phase-averaged results in figure 12(*c*) display relatively lower spanwise velocity magnitudes than the instantaneous snapshots, it can be concluded that the strongest velocity fluctuations in the aft portion of the LSB are associated with random vortex deformations and breakdown. Comparing the results

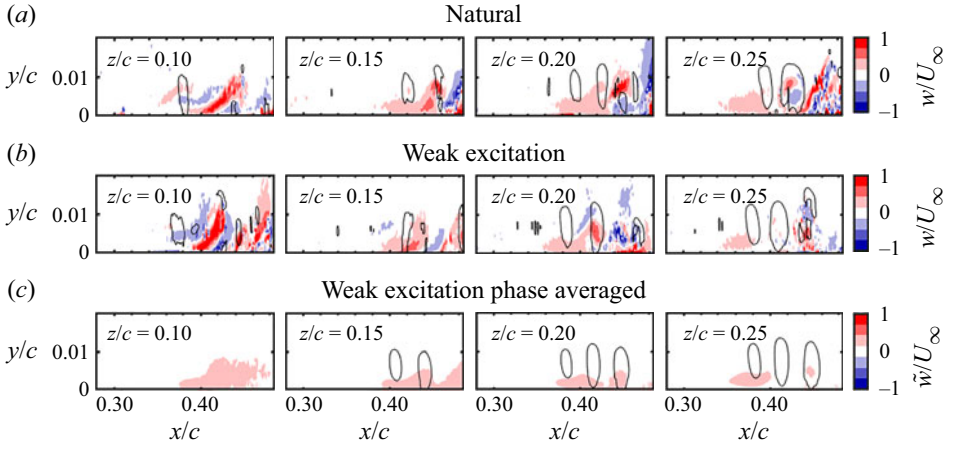

Figure 12. Spanwise velocity contours at the four side-view planes closest to the wing root: (*a*) uncorrelated snapshots from natural flow, (*b*) phase-locked snapshots from weakly excited flow and (*c*) phase average from weakly excited flow.

from the plane at $z/c = 0.10$ with the planes farther from the wing root, it is apparent that stronger spanwise velocity fluctuations occur farther upstream at $z/c = 0.10$. This suggests that the more rapid vortex breakdown seen at $z/c = 0.10$ (figure 11) is caused by an earlier onset of three-dimensional vortex deformations, likely linked to substantial mean spanwise flow in the junction region (figure 5*b*).

The streamwise growth of velocity fluctuations in the LSB is explored in figure 13, which presents contours of turbulent kinetic energy (TKE) at $y = \delta_x^*$. The streamwise location of maximum streamwise displacement thickness is shown by the stars, which provide an indication of the mean transition location. Downstream of the maximum streamwise displacement thickness, a substantial increase in TKE occurs due to the shedding of coherent structures (figure 11) and their subsequent breakdown to turbulence. The spanwise variations in the streamwise locations of separation and reattachment are similar to the variations in the location of maximum streamwise displacement thickness and the contours of TKE. In the junction region, the upstream shift in reattachment at $z/c = 0.10$ is accompanied by an earlier initial growth of velocity fluctuations, implying that the transition process is substantially influenced by end effects in the junction region.

Figures 13(*b*)–13(*d*) present the growth of each of the three components of velocity fluctuations along $y = \delta_x^*$ for the four stereo-PIV measurement planes closest to the wing root. The results reveal that the earlier growth in TKE at $z/c = 0.10$ is the result of earlier growth in all three fluctuating velocity components, occurring at comparable initial growth rates to the planes farther from the wing root. The exponential growth of wall-normal velocity fluctuations in the streamwise direction is consistent with that expected from a linear convective instability mechanism. The similarity in the growth rates between the four planes suggests that the primary instability mode is not affected significantly in the junction region. Instead, the earlier appearance of more significant velocity fluctuations in the separated shear layer is likely the result of an increase in the initial amplitude of perturbations. This is substantiated by the streamwise velocity fluctuations in figure 13(*b*), which indicate that the largest amplitudes in the forward part of the LSB occur at $z/c = 0.10$. Thus, although the test section wall turbulent boundary layer is relatively thin (figure 2), its presence introduces higher-amplitude perturbations away from the root, leading to the earlier appearance of significant streamwise and wall-normal

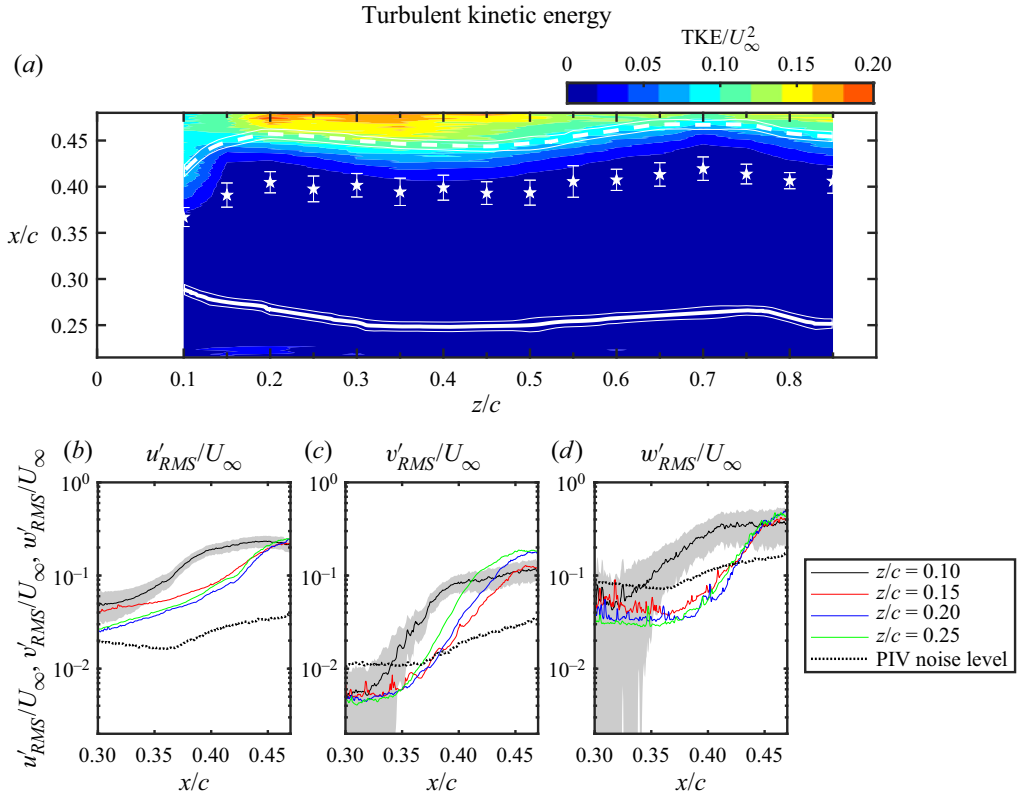

Figure 13. (*a*) Contours of TKE at $y = \delta^*_x$. Thick solid line: separation line; thick dashed line: reattachment line; thin solid lines: uncertainty in separation and reattachment lines; stars: streamwise location of maximum δ^*. (*b*)–(*d*) RMS fluctuating velocity components at $y = \delta^*_x$. Shaded area indicates typical uncertainty.

shear layer fluctuations (figures 13(*b*) and 13(*c*)) at $z/c = 0.10$ and earlier shear layer roll-up. Note that, in contrast to the streamwise fluctuations (figure 13*b*) which saturate at similar amplitudes along the span, the maximum amplitude of wall-normal velocity fluctuations is reduced at the two planes closest to the wing root ($z/c = 0.10$ and 0.15, figure 13*c*). Here, the closer proximity of the separated shear layer to the wing surface near the wing root (figure 8) is expected to limit the maximum amplitude of wall-normal velocity fluctuations in the junction region. Because the wall-normal velocity fluctuations that occur near reattachment are related to the passage of spanwise shear layer vortices, the reduction in wall-normal velocity fluctuations near the wing root also points to a change in the vortex shedding dynamics in the junction region. This is also highlighted by the significantly earlier onset of spanwise velocity fluctuations at $z/c = 0.10$, consistent with the earlier breakdown of the rollers seen in figure 11 at this plane.

The development of shear layer vortices shed from the LSB across the wingspan is investigated further using the top-view PIV configuration. Instantaneous top-view snapshots of streamwise velocity for the natural and weakly excited flows are presented in figure 14. As the top-view light sheet was positioned to intersect the top halves of the shear layer vortices, the spanwise bands of increased streamwise velocity seen in the figure identify the location of the vortices. The vortical structures seen in both the natural (figure 14*a*) and weakly excited flows (figure 14*b*) share similar features, although vortices appear to persist slightly farther downstream in the weakly excited flow.

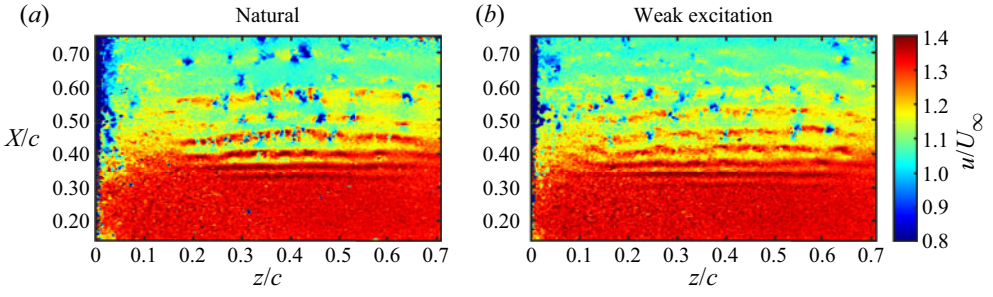

Figure 14. Instantaneous snapshots of streamwise velocity from top-view PIV.

Up to the location of mean transition ($X/c \approx 0.40$), the vortices are strongly uniform along the span for $z/c \gtrsim 0.20$. However, farther downstream, the dominant structures rapidly lose spanwise coherence as they undergo three-dimensional deformations. Within the junction region ($z/c \leq 0.20$), shear layer vortices become progressively difficult to identify.

Proper orthogonal decomposition (POD) was performed on the streamwise velocity fluctuations measured using the top-view PIV configuration based on the method of snapshots (Sirovich 1987) to obtain a statistical description of spanwise vortex development in the LSB. The energy of the first 20 POD modes for the natural and weakly excited flows is plotted in figure 15(*a*) in terms of the spatially averaged TKE of each mode. The two most energetic modes of the natural and weakly excited flows contain substantially more energy than the higher modes and display similar spatial distributions that are offset in the streamwise direction by 1/4 of the fundamental wavelength, which is indicative of mode pairing. Thus, the first mode pair describes the convection of dominant coherent structures in the aft portion of the LSB (e.g. Ben Chiekh *et al.* 2004; Lengani *et al.* 2014). For brevity, the spatial distribution of only the most energetic mode is presented in figures 15(*b*) and 15(*c*) for the natural and weakly excited flows, respectively. The spatial mode contours reveal similar spanwise vortex development in both the natural and weakly excited flows. Although the weak excitation leads to shed vortices persisting farther downstream of the LSB, the shape and spanwise extent of the spatial mode remains similar, confirming the decay in the modal magnitude for $z/c < 0.20$, and indicating a notable deformation of the vortex cores between $z/c = 0.1$ and $z/c = 0.2$, which is more pronounced in figure 15(*c*). However, because similar vortex undulations have also been observed in two-dimensional LSBs (e.g. McAuliffe & Yaras 2005; Kurelek *et al.* 2021), this cannot be conclusively attributed to end effects.

A statistical comparison of vortex development at different spanwise locations is facilitated using POD of the velocity data from each side-view measurement plane in the natural flow, also obtained using the method of snapshots. Figure 16 presents the spatially averaged TKE of the 20 most energetic modes at each plane, enabling a comparison of modal energy between measurement planes. The similar energy content of the first two modes at each plane is indicative of mode pairing. This was verified by inspection of the spatial mode shapes. The fluctuations in the relative energy content of the most energetic mode pair along the span correlates with the spanwise changes in the mean reattachment point (figure 6) and TKE (figure 13*a*), linked to the changes in the shear layer roll-up location. Specifically, the earlier roll-up and transition, which lead to the upstream advancement of reattachment and earlier TKE saturation, is associated with greater energy of the dominant mode pair in figure 16. Consistently, a notable increase in the energy of

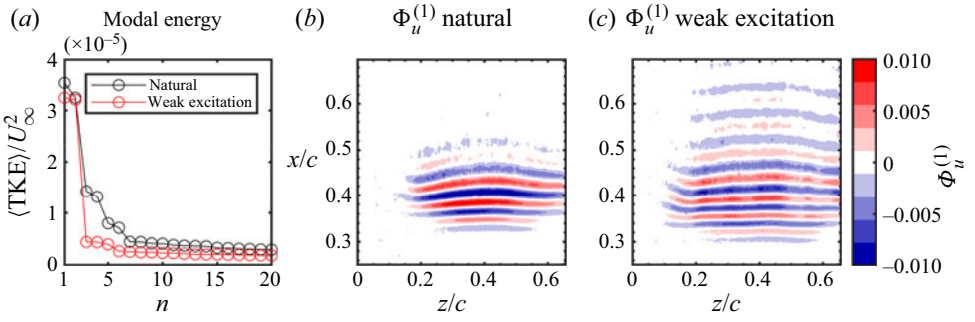

Figure 15. (*a*) POD modal energy of streamwise velocity fluctuations from top-view PIV. (*b*), (*c*) Dominant spatial POD modes for natural and weakly excited flow.

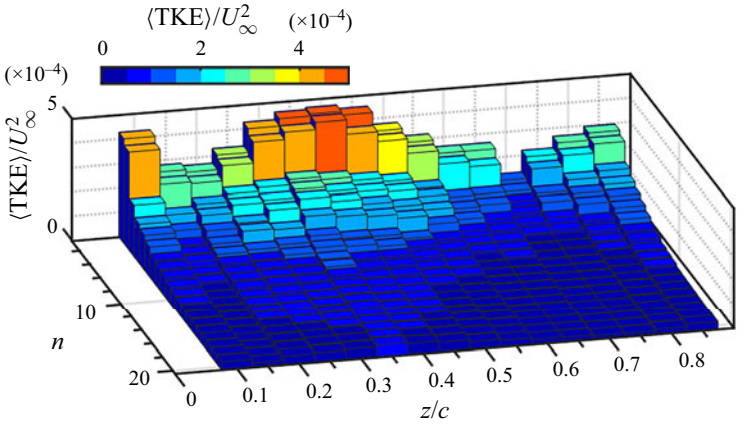

Figure 16. Spatially averaged TKE of the first 20 POD modes at each side-view measurement plane.

the two most energetic modes occurs at the plane closest to the wing root, where earlier shear layer shedding takes place.

Figure 17 depicts the streamwise, wall-normal and spanwise components of the first POD mode for the four planes closest to the wing root. The second mode is also shown for $z/c = 0.25$ to illustrate the spatial topologies of the paired first and second modes, which is typical of the other planes shown. Note that the spatial modes are multiplied by $\sqrt{\langle TKE \rangle}$, which allows for a direct comparison of modal velocity fluctuation magnitudes between planes. At all planes, a streamwise periodic pattern is seen in the aft portion of the bubble. At $z/c = 0.25$, which is representative of the planes farther from the wing root, the x and y components of $\Phi^{(1)}$ and $\Phi^{(2)}$ are typical of those obtained from PIV measurements of two-dimensional LSBs (e.g. Lengani *et al.* 2014; Kurelek *et al.* 2019) and correspond to spanwise vortices shed from the separated shear layer (figure 11), which produce strong streamwise and wall-normal velocity fluctuations. The spanwise modal velocity fluctuations are attributed to the consistent occurrence of three-dimensional vortex deformations at constant spanwise locations, similar to those observed in two-dimensional LSBs (e.g. Kurelek *et al.* 2021). In the junction region ($z/c \leq 0.20$), the magnitudes of the wall-normal velocity fluctuations of the first POD mode progressively diminish as the wing root is approached, consistent with the reduction in the maximum amplitude of wall-normal RMS velocity fluctuations (figure 13*c*).

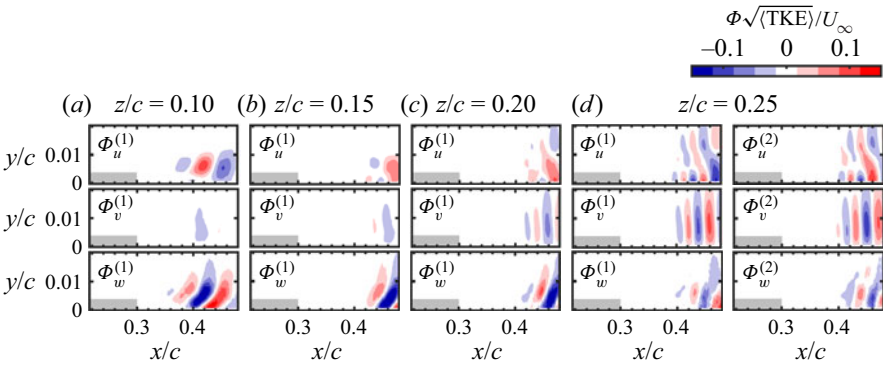

Figure 17. Spatial distribution of selected POD modes at the four planes nearest to the wing root. The shaded area has been excluded from the POD due to high uncertainty in the thin upstream boundary layer.

In addition, an increase in the magnitudes of the spanwise component of the modes occurs near the wing root, most prominently at $z/c = 0.10$ (figure 17*a*), substantiating the previous observation that an increase in the level of spanwise velocity fluctuations occurs near the wing root. There is also a notable change in the modal shape components, with streamwise mode shape at $z/c = 0.10$ becoming similar to wall-normal mode shapes seen farther outboard. The observed changes in the first mode shape topologies and magnitudes suggest that vortex core reorientation occurs in the junction region. The spatial correlation between opposite signs of streamwise ($\Phi_u^{(1)}$) and spanwise ($\Phi_w^{(1)}$) components at $z/c = 0.10$ (figure 17*a*) suggests that the vortex cores tilt into the negative y direction in the junction region, which is consistent with the reduction in height of the LSB in the junction region.

A comparison of the phase-averaged vortex shedding obtained from the top and side views is presented in figure 18. Figure 18(*a*) presents contours of phase-averaged streamwise velocity ($\tilde{u}$) from the top view, whereas figure 18(*b*) presents contours of λ_2 criterion (Jeong & Hussain 1995) obtained from the volumetric reconstruction of side-view measurement planes at the same phase angle. The full cycle sequence of figure 18(*a*) is available in Movie 2. Consistent with the instantaneous snapshots (figure 14) and POD results (figure 15), the phase-averaged results reveal largely two-dimensional periodic vortex shedding outside of the junction region. This confirms the association between the bands of high streamwise velocity in the top-view measurements with the vortices observed in the side-view planes. Within the junction region ($z/c \leq 0.20$), identification of vortices becomes progressively more difficult. The absence of clearly defined phase-averaged vortices near $z/c = 0.10$ in both figures 18(*a*) and 18(*b*) is attributed to significant cycle-to-cycle variations in the shedding process that result in phase smearing.

To better understand the changes in vortex shedding across the span, vortex identification was employed. Vortex core locations were defined as local minima of λ_2 criterion with a minimum prominence of $1500U_\infty^2/c^2$. Figure 19(*a*) presents the locations of all vortex cores identified in the four planes closest to the wing root in the natural flow case. At all planes, the identified vortex cores are clustered around the streamwise displacement thickness (dashed line) in the aft portion of the LSB, illustrating that the roll-up occurs primarily in the vicinity of the maximum bubble height location. The reduction in LSB thickness in the junction region (figure 8) causes a decrease in the wall normal distance of vortex cores from the wing surface. Consistent with the earlier growth

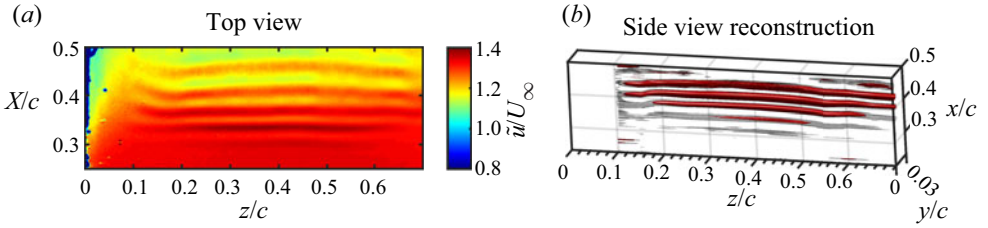

Figure 18. (*a*) Phase-averaged streamwise velocity contours from top-view PIV of weakly excited flow. Full cycle sequence available in Movie 2. (*b*) Isosurfaces of λ_2 reconstructed from side-view phase-averaged PIV of weakly excited flow. Grey: $\lambda_2 c^2/U_\infty^2 = -100$, red: $\lambda_2 c^2/U_\infty^2 = -500$.

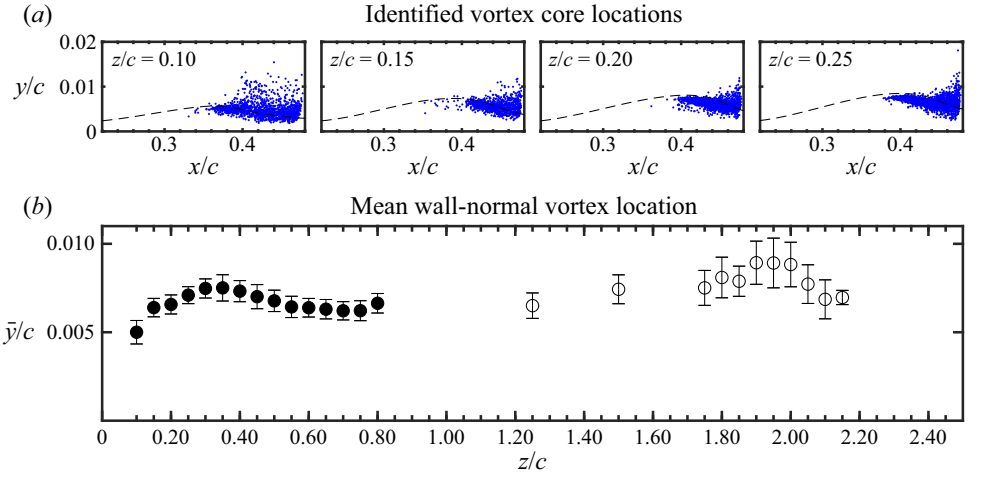

Figure 19. (*a*) Locations of identified vortex cores at selected planes. Dashed line: δ_x^*. (*b*) Mean wall-normal vortex core position within a window of $0.01c$ of the x location of maximum δ_x^*. Solid markers: present study; open markers: Toppings & Yarusevych (2021).

of velocity fluctuations closer to the wing root (figure 13), vortices form progressively farther upstream for $z/c \leq 0.15$ compared with the planes closer to the midspan. In addition, the variability of vortex core locations in the wall-normal direction increases notably in the same region.

The mean wall-normal vortex core location at the x location of maximum streamwise displacement thickness is plotted in figure 19(*b*) for the entire span of the wing based on the data from the present study and that from Toppings & Yarusevych (2021) near the wing tip. The error bars indicate one standard deviation of the wall-normal vortex core locations. Comparing figures 8 and 19(*b*), it is apparent that the distance of the vortex cores from the wing surface displays similar trends to the LSB thickness. Near the midspan of the wing, the wall-normal distance of the vortex cores is relatively uniform between the local maxima that occur at $z/c = 0.35$ and 1.90. At the wing root and tip, a reduction in wall-normal vortex core distance is observed. The substantial decrease in wall-normal vortex core location in the junction region provides further evidence for vortex core tilting towards the wing surface.

The frequency content of velocity fluctuations in the LSB was investigated using the high-speed top-view PIV configuration in the natural flow. Figure 20 presents the variation of power spectral density of streamwise velocity fluctuations across the span.

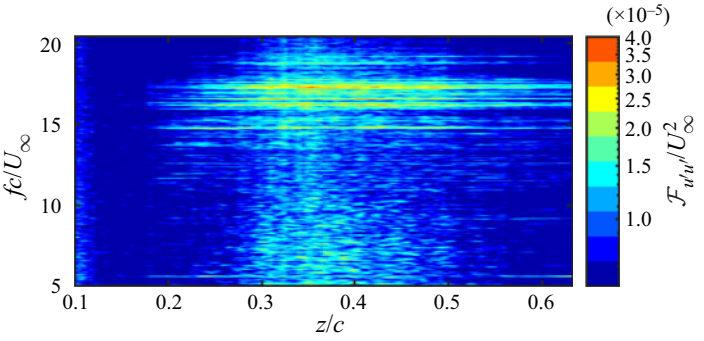

Figure 20. Spectral analysis of streamwise velocity fluctuations.

The spectral analysis was performed using Welch's method with a window size of 2^7 samples.

The spectra presented were obtained by averaging the power spectral density over $0.35 \leq x/c \leq 0.5$ at each z location, i.e. within the region where prominent vortex shedding is observed. The resulting uncertainty in power spectral density is less than 23 %, and the frequency resolution is $0.3U_\infty/c$. For $z/c > 0.20$, spectral energy is concentrated within the band of frequencies in the range $15.6 < fc/U_\infty < 17.9$. This frequency range is in good agreement with the central shear layer instability frequencies reported for the same wing model and flow conditions in Toppings *et al.* (2021), and is similar to that expected for natural transition in the separated shear layer (e.g. Hain *et al.* 2009). Outside of the junction region, the dominant energy content of velocity fluctuations remains centred at $fc/U_\infty \approx 16$, suggesting that the primary instability mode in the midspan region of the wing is largely unmodified by root effects. Although the relative breadth of the spectral content around the central frequency points to cycle-to-cycle variations in the shedding process, the spanwise uniformity of the spectral results indicates that the vortex shedding frequency does not change substantially along the span for $z/c > 0.20$. For $z/c < 0.20$, a rapid decay of velocity fluctuations around $fc/U_\infty = 16$ is seen, with no significant spectral peaks seen at or beyond $z/c \approx 0.15$. This is partly attributed to the deformation and earlier breakdown of vortices in this region, and the decrease in LSB thickness in the junction region which shifts the shear layer closer to the surface and away from the PIV measurement plane.

The influence of the wing root junction on the LSB transition dynamics is also seen in the spanwise changes that occur to the streamwise vortex shedding wavelength. Streamwise wavelength spectra of wall-normal ($\widehat{\mathcal{F}_{v'v'}}$) and spanwise ($\widehat{\mathcal{F}_{w'w'}}$) velocity fluctuations from each side-view measurement plane are presented in figures 21(*a*) and 21(*b*), respectively. The spectra presented were obtained by averaging the power spectra from each instantaneous velocity field snapshot over 1000 snapshots obtained at a given z/c plane. The relative uncertainty in the averaged power spectral density is less than 7 % and the wavelength resolution at a given wavelength (λ) is equal to $\lambda^2/(0.125c)$. Each spectrum has been normalised by total energy and shifted by an order of magnitude for clarity. Similar to the frequency analysis from the top view, the wavelength of the spectral peaks in both velocity fluctuation spectra is largely uniform away from the wing root. The mean wavelength of the spectral peaks is $\lambda/c = 0.039$, which agrees with the spacing between consecutive vortices in figures 11 and 12. In the junction region ($z/c \leq 0.20$), the reduction in relative magnitude and broadening of the spectral peak of

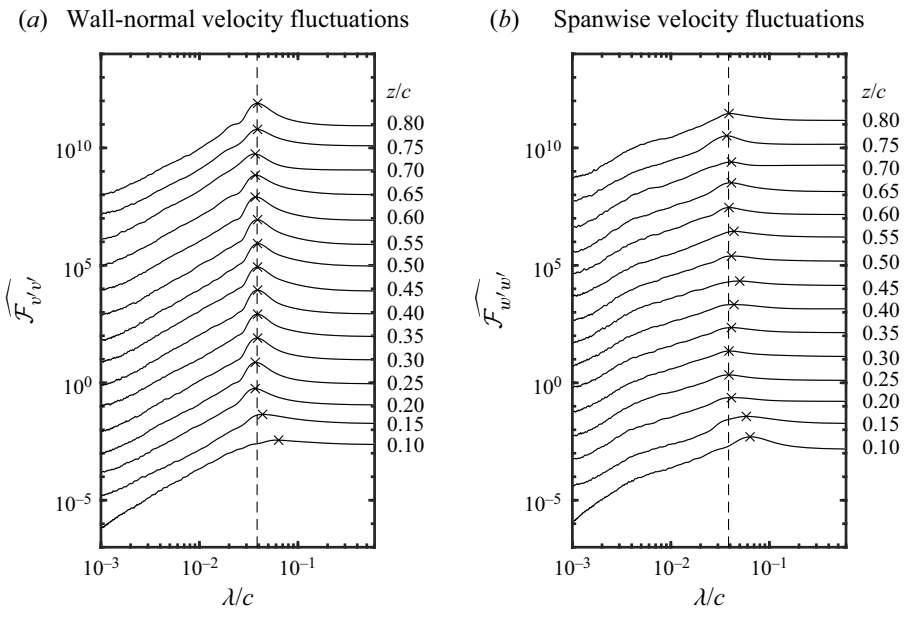

Figure 21. Streamwise wavelength spectra. All spectra have been normalised by total energy and each z/c location has been shifted an order of magnitude for clarity. Dashed line: $\lambda/c = 0.039$; x markers: maximum normalised power spectral density.

wall-normal fluctuations (figure 21*a*) is accompanied by an increase in relative magnitude of the spectral peak of spanwise velocity fluctuations (figure 21*b*) in agreement with the change in the dominant components of coherent velocity fluctuations seen in the POD spatial modes at the planes near the wing root (figure 17) and increase in spanwise velocity fluctuations (figures 11 and 12) attributed to vortex deformations and earlier breakdown. The spectral results also indicate that the fundamental streamwise vortex shedding wavelength increases in the junction region to $\lambda/c = 0.060$ at $z/c = 0.10$. It is speculated that this change in wavelength may be a result of vortex core reorientation in the junction region. In contrast, measurements near the wing tip do not show evidence of vortex core reorientation or a change in the fundamental wavelength (Toppings & Yarusevych 2021, figure 24(*a*)). Therefore, both the mean flow and the vortex dynamics in immediate proximity to the ends of the LSB on a finite wing are affected by the type of end condition imposed.

The foregoing discussion of vortex shedding characteristics shows that, similar to the mean LSB structure, shear layer transition and vortex shedding dynamics are largely unaffected by the presence of the wing root outside of the junction region ($z/c > 0.20$). In the midspan region of the wing, the transitioning separated shear layer rolls up into largely two-dimensional spanwise vortices near the location of maximum displacement thickness, and spanwise variations in the frequency and wavelength of shear layer vortex shedding are relatively small. Within the junction region ($z/c \leq 0.20$), shear layer transition is affected by the presence of the test section wall boundary layer and spanwise flow, which increases the initial amplitudes of perturbations in the separated laminar shear layer leading to earlier vortex roll-up. Large spanwise velocity magnitudes in the junction region point to vortex deformations and more rapid vortex breakdown, leading to earlier reattachment. As a result of these changes to the LSB dynamics, the streamwise and wall-normal extent of the LSB is substantially reduced near the wing root. This is in contrast to the LSB behaviour near

the wing tip, where a delay in vortex roll-up and breakdown causes a lengthening of the reverse flow region (Toppings & Yarusevych 2021).

4. Concluding remarks

An experimental investigation of an LSB near a wing root junction was conducted on a semispan NACA 0018 wing at an angle of attack of $\alpha = 6^\circ$ and a chord Reynolds number of $Re_c = 1.25 \times 10^5$. The flowfield of the separation bubble forming on the suction surface of the wing near the wing root has been explored using surface pressure measurements, PIV and surface oil flow visualisation.

Between the root and tip end effected regions, the LSB on the wing is similar to that observed on a two-dimensional airfoil geometry at an equivalent effective angle of attack. The transition process near the midspan leads to the roll-up of the separated laminar shear layer into spanwise vortices that subsequently undergo breakdown to turbulence. Away from the wing root, the shear layer vortices are similar to those observed in two-dimensional experiments, and the vortex shedding wavelength and frequency is largely constant in the spanwise direction. Therefore, the interaction between root and tip effects at the present aspect ratio is deemed to be insignificant.

The results show that the influence of the wing root junction on the LSB extends well beyond the test section wall boundary layer thickness up to approximately $0.5c$ from the wing root. In close proximity to the wing root junction, the separation bubble thickness and length are substantially reduced. The LSB in the junction region is open, and spanwise flow enters the bubble at its end. Between $0.2c$ and $0.5c$ from the wing root, the LSB becomes notably thicker and a reduction in spanwise flow occurs with increasing distance from the wing root.

In the junction region, higher initial perturbation amplitudes lead to earlier vortex roll-up, and end effects lead to more significant vortex deformations and earlier breakdown. Consistently, the LSB moves upstream and both its height and length reduce near the wing root.

The dynamics of the spanwise roll-up vortices in the junction region is notably different from that occurring near the wing tip, where a progressive delay in shear layer roll-up is observed with increasing z/c (Toppings & Yarusevych 2021). At the wing root, vortex shedding starts earlier upstream and is accompanied by notable vortex deformations and subsequent earlier breakdown. These differences in vortex dynamics between the root and tip result in opposite changes to the streamwise location of transition and reattachment, which shift upstream near the wing root, and downstream near the wing tip. Despite these differences in transition dynamics, the LSB is open at both ends, drawing in the fluid from the surrounding flow. The magnitude of the spanwise volume flow rate within the LSB reaches local maxima near both the wing root and tip, and diminishes towards the midspan of the wing. Regions of increased LSB thickness occur near both end regions, suggesting that localised bubble thickening is a common feature of open LSBs near different types of end conditions. Although the wing root junction substantially influences LSB development in its vicinity, junction effects are more localised than tip effects, the latter influencing the spanwise pressure gradient over a larger portion of the wingspan.

Supplementary movies. Supplementary movies are available at https://doi.org/10.1017/jfm.2022.460.

Acknowledgements. The authors thank Mr D. Patel for developing the oil flow visualisation technique and Mr Q. Qin for assisting with the experiments.

Funding. The authors gratefully acknowledge the Natural Sciences and Engineering Research Council of Canada for funding this work.

Declaration of interests. The authors report no conflict of interest.

Author ORCIDs.
Serhiy Yarusevych https://orcid.org/0000-0003-2723-2744.

References

ALAM, M. & SANDHAM, N.D. 2000 Direct numerical simulation of 'short' laminar separation bubbles with turbulent reattachment. *J. Fluid Mech.* **403**, 223–250.

AVANCI, M.P., RODRÍGUEZ, D. & ALVES, L.S. DE B. 2019 A geometrical criterion for absolute instability in separated boundary layers. *Phys. Fluids* **31** (1), 014103.

AWASTHI, M., MOREAU, D.J. & DOOLAN, C.J. 2018 Flow structure of a low aspect ratio wall-mounted airfoil operating in a low Reynolds number flow. *Expl Therm. Fluid Sci.* **99**, 94–116.

BASTEDO, W.G. & MUELLER, T.J. 1986 Spanwise variation of laminar separation bubbles on wings at low Reynolds number. *J. Aircraft* **23** (9), 687–694.

BEN CHIEKH, M., MICHARD, M., GROSJEAN, N. & BÉRA, J.-C. 2004 Reconstruction temporelle d'un champ aérodynamique instationnaire à partir de mesures PIV non résolues dans le temps. 9e Congrès Francophone de Vélocimétrie Laser paper D.8.

BOUTILIER, M.S.H. & YARUSEVYCH, S. 2012 Effects of end plates and blockage on low-Reynolds-number flows over airfoils. *AIAA J.* **50** (7), 1547–1559.

BRENDEL, M. & MUELLER, T.J. 1988 Boundary-layer measurements on an airfoil at low Reynolds numbers. *J. Aircraft* **25** (7), 612–617.

BURGMANN, S., DANNEMANN, J. & SCHRÖDER, W. 2008 Time-resolved and volumetric PIV measurements of a transitional separation bubble on an SD7003 airfoil. *Exp. Fluids* **44** (4), 609–622.

CARMICHAEL, B.H. 1981 Low Reynolds number airfoil survey. *Tech. Rep.* NASA CR-165803. Low Energy Transportation Systems.

CHEN, Z.J., QIN, N. & NOWAKOWSKI, A.F. 2013 Three-dimensional laminar-separation bubble on a cambered thin wing at low Reynolds numbers. *J. Aircraft* **50** (1), 152–163.

DELAFIN, P.L., DENISET, F. & ASTOLFI, J.A. 2014 Effect of the laminar separation bubble induced transition on the hydrodynamic performance of a hydrofoil. *Eur. J. Mech.* B/*Fluids* **46**, 190–200.

DEVENPORT, W.J. & SIMPSON, R.L. 1990 Time-dependent and time-averaged turbulence structure near the nose of a wing–body junction. *J. Fluid Mech.* **210** (23), 23–55.

DIWAN, S.S. & RAMESH, O.N. 2009 On the origin of the inflectional instability of a laminar separation bubble. *J. Fluid Mech.* **629**, 263–298.

FLEMING, J.L., SIMPSON, R.L., COWLING, J.E. & DEVENPORT, W.J. 1993 An experimental study of a turbulent wing–body junction and wake flow. *Exp. Fluids* **14** (5), 366–378.

GAND, F., DECK, S., BRUNET, V. & SAGAUT, P. 2010 Flow dynamics past a simplified wing body junction. *Phys. Fluids* **22** (11), 115111.

GASTER, M. 1967 The Structure and Behaviour of Laminar Separation Bubbles. *Tech. Rep.* Aeronautical Research Council Reports and Memoranda 3595.

HÄGGMARK, C.P., BAKCHINOV, A.A. & ALFREDSSON, P.H. 2000 Experiments on a two–dimensional laminar separation bubble. *Phil. Trans. R. Soc. Lond.* A **358** (1777), 3193–3205.

HAIN, R., KÄHLER, C.J. & RADESPIEL, R. 2009 Dynamics of laminar separation bubbles at low-Reynolds-number aerofoils. *J. Fluid Mech.* **630**, 129–153.

HODSON, H.P. & HOWELL, R.J. 2005 The role of transition in high-lift low-pressure turbines for aeroengines. *Prog. Aerosp. Sci.* **41** (6), 419–454.

HORTON, H.P. 1968 Laminar separation bubbles in two and three dimensional incompressible flow. Ph.D. thesis, University of London.

HOSSEINVERDI, S. & FASEL, H.F. 2019 Numerical investigation of laminar–turbulent transition in laminar separation bubbles: the effect of free-stream turbulence. *J. Fluid Mech.* **858**, 714–759.

HUANG, R.F. & LIN, C.L. 1995 Vortex shedding and shear-layer instability of wing at low-Reynolds numbers. *AIAA J.* **33** (8), 1398–1403.

JEONG, J. & HUSSAIN, F. 1995 On the identification of a vortex. *J. Fluid Mech.* **285**, 69–94.

KIRK, T.M. & YARUSEVYCH, S. 2017 Vortex shedding within laminar separation bubbles forming over an airfoil. *Exp. Fluids* **58** (5), 43.

KREMHELLER, A. & FASEL, H. 2010 Water tunnel experiments on three dimensional separation bubbles on a flat plate. In *40th Fluid Dynamics Conference and Exhibit*, p. 4738. American Institute of Aeronautics and Astronautics.

KURELEK, J.W., TUNA, B.A., YARUSEVYCH, S. & KOTSONIS, M. 2021 Three-dimensional development of coherent structures in a two-dimensional laminar separation bubble. *AIAA J.* **59** (2), 493–505.

KURELEK, J.W., YARUSEVYCH, S. & KOTSONIS, M. 2019 Vortex merging in a laminar separation bubble under natural and forced conditions. *Phys. Rev. Fluids* **4** (6), 063903.

LAMBERT, A. & YARUSEVYCH, S. 2019 Effect of angle of attack on vortex dynamics in laminar separation bubbles. *Phys. Fluids* **31** (6), 064105.

LENGANI, D., SIMONI, D., UBALDI, M. & ZUNINO, P. 2014 POD analysis of the unsteady behavior of a laminar separation bubble. *Expl Therm. Fluid Sci.* **58**, 70–79.

MARXEN, O., KOTAPATI, R.B., MITTAL, R. & ZAKI, T. 2015 Stability analysis of separated flows subject to control by zero-net-mass-flux jet. *Phys. Fluids* **27** (2), 024107.

MARXEN, O., LANG, M. & RIST, U. 2013 Vortex formation and vortex breakup in a laminar separation bubble. *J. Fluid Mech.* **728**, 58–90.

MCAULIFFE, B.R. & YARAS, M.I. 2005 Separation-bubble-transition measurements on a low-Re airfoil using particle image velocimetry. In *Volume 3: Turbo Expo 2005, Parts A and B*, pp. 1029–1038. ASMEDC.

MICHALKE, A. 1991 On the instability of wall-boundary layers close to separation. In *Separated Flows and Jets* (ed. V. Kozlov & A.V. Dovgal), pp. 557–564. Springer.

MICHELIS, T., YARUSEVYCH, S. & KOTSONIS, M. 2018 On the origin of spanwise vortex deformations in laminar separation bubbles. *J. Fluid Mech.* **841**, 81–108.

MIOZZI, M., CAPONE, A., COSTANTINI, M., FRATTO, L., KLEIN, C. & DI FELICE, F. 2019 Skin friction and coherent structures within a laminar separation bubble. *Exp. Fluids* **60** (1), 13.

MOREAU, D.J. & DOOLAN, C.J. 2016 Tonal noise production from a wall-mounted finite airfoil. *J. Sound Vib.* **363**, 199–224.

MUELLER, T.J. & DELAURIER, J.D. 2003 Aerodynamics of small vehicles. *Annu. Rev. Fluid Mech.* **35** (1), 89–111.

NATI, A., DE KAT, R., SCARANO, F. & VAN OUDHEUSDEN, B.W. 2015 Dynamic pitching effect on a laminar separation bubble. *Exp. Fluids* **56** (9), 172.

O'MEARA, M.M. & MUELLER, T.J. 1987 Laminar separation bubble characteristics on an airfoil at low Reynolds numbers. *AIAA J.* **25** (8), 1033–1041.

PAULEY, L.L., MOIN, P. & REYNOLDS, W.C. 1990 The structure of two-dimensional separation. *J. Fluid Mech.* **220**, 397–411.

PELLETIER, A. & MUELLER, T.J. 2001 Effect of endplates on two-dimensional airfoil testing at low Reynolds number. *J. Aircraft* **38** (6), 1056–1059.

RIST, U. & MAUCHER, U. 2002 Investigations of time-growing instabilities in laminar separation bubbles. *Eur. J. Mech.* B/*Fluids* **21** (5), 495–509.

ROACH, P.E. & TURNER, J.T. 1985 Secondary loss generation by gas turbine support struts. *Intl J. Heat Fluid Flow* **6** (2), 79–88.

RODRÍGUEZ, D. & GENNARO, E.M. 2019 Enhancement of disturbance wave amplification due to the intrinsic three-dimensionalisation of laminar separation bubbles. *Aeronaut. J.* **123** (1268), 1492–1507.

RODRÍGUEZ, D., GENNARO, E.M. & JUNIPER, M.P. 2013 The two classes of primary modal instability in laminar separation bubbles. *J. Fluid Mech.* **734**, 1–11.

RODRÍGUEZ, D. & THEOFILIS, V. 2010 Structural changes of laminar separation bubbles induced by global linear instability. *J. Fluid Mech.* **655**, 280–305.

SCARANO, F. & RIETHMULLER, M.L. 2000 Advances in iterative multigrid PIV image processing. *Exp. Fluids* **29** (7), S051–S060.

SCHULZ, H.D., GALLUS, H.E. & LAKSHMINARAYANA, B. 1990 Three-dimensional separated flow field in the endwall region of an annular compressor cascade in the presence of rotor-stator interaction. Part 1. Quasi-steady flow field and comparison with steady-state data. *Trans. ASME J. Turbomach.* **112** (4), 669–678.

SCIACCHITANO, A. & WIENEKE, B. 2016 PIV uncertainty propagation. *Meas. Sci. Technol.* **27** (8), 084006.

SELIG, M., DETERS, R. & WILIAMSON, G. 2011 Wind tunnel testing airfoils at low Reynolds numbers. In *49th AIAA Aerospace Sciences Meeting including the New Horizons Forum and Aerospace Exposition*, p. 875. *AIAA Paper* 2011-875.

SIEVERDING, C.H. & VAN DEN BOSCHE, P. 1983 The use of coloured smoke to visualize secondary flows in a turbine-blade cascade. *J. Fluid Mech.* **134**, 85–89.

SIMONI, D., LENGANI, D., UBALDI, M., ZUNINO, P. & DELLACASAGRANDE, M. 2017 Inspection of the dynamic properties of laminar separation bubbles: free-stream turbulence intensity effects for different Reynolds numbers. *Exp. Fluids* **58** (6), 66.

SIMPSON, R.L. 2001 Junction flows. *Annu. Rev. Fluid Mech.* **33** (1), 415–443.

SIROVICH, L. 1987 Turbulence and the dynamics of coherent structures. I. Coherent structures. *Q. Appl. Maths* **45** (3), 561–571.

SURANA, A., GRUNBERG, O. & HALLER, G. 2006 Exact theory of three-dimensional flow separation. Part 1. Steady separation. *J. Fluid Mech.* **564**, 57–103.

TANI, I. 1964 Low-speed flows involving bubble separations. *Prog. Aerosp. Sci.* **5**, 70–103.

TOBAK, M. & PEAKE, D.J. 1982 Topology of three-dimensional separated flows. *Annu. Rev. Fluid Mech.* **14** (1), 61–85.

TOPPINGS, C.E., KURELEK, J.W. & YARUSEVYCH, S. 2021 Laminar separation bubble development on a finite wing. *AIAA J.* **59** (8), 2855–2867.

TOPPINGS, C.E. & YARUSEVYCH, S. 2021 Structure and dynamics of a laminar separation bubble near a wingtip. *J. Fluid Mech.* **929**, A39.

TRAUB, L.W. & COOPER, E. 2008 Experimental investigation of pressure measurement and airfoil characteristics at low Reynolds numbers. *J. Aircraft* **45** (4), 1322–1333.

WATMUFF, J.H. 1999 Evolution of a wave packet into vortex loops in a laminar separation bubble. *J. Fluid Mech.* **397**, 119–169.

WELCH, P. 1967 The use of fast Fourier transform for the estimation of power spectra: a method based on time averaging over short, modified periodograms. *IEEE Trans. Audio and Electroacoust.* **15** (2), 70–73.

WESTERWEEL, J. & SCARANO, F. 2005 Universal outlier detection for PIV data. *Exp. Fluids* **39** (6), 1096–1100.

WIENEKE, B. 2005 Stereo-PIV using self-calibration on particle images. *Exp. Fluids* **39** (2), 267–280.

WIENEKE, B. 2015 PIV uncertainty quantification from correlation statistics. *Meas. Sci. Technol.* **26** (7), 074002.

WOOD, D.H. & WESTPHAL, R.V. 1992 Measurements of the flow around a lifting-wing/body junction. *AIAA J.* **30** (1), 6–12.